Christian-Albrechts-University of Kiel

Faculty of Mathematics and Natural Sciences

Institute of Theoretical Physics and Astrophysics

Computational Solid-State Theory Group of F.Caruso

AB-INITIO STUDY ON THE ELECTRONIC
PROPERTIES OF TRIGONAL TELLURIUM

Bachelor Thesis

to obtain the degree 'Bachelor of Science'

Author:	Jan-Niklas Mohr
Study subject:	Physics/Bachelor, 1-Subject
Semester:	9
Stu-Email-Adress:	stu217072@mail.uni-kiel.de
Matriculation number:	1138269

Deadline:	December 09, 2022
First reviewer:	Prof. Dr. Fabio Caruso
Second reviewer:	Prof. Dr. Michael Bonitz

'[...]Maybe I'm mistaken expecting you to fight
Or maybe I'm just crazy, I don't know wrong from right
But while I am still living, I've just got this to say
It's always up to you if you want to be that
Want to see that want to see that way
You're coming along'
- Lyrics of the song 'School' by Supertramp (1974) -

Zusammenfassung

In dieser Arbeit geht es um ab-initio Berechnungen der Bandstruktur von trigonalem Tellur. Dazu wurde das open-source Programm Quantum ESPRESSO verwendet. Das methodische Vorgehen bestand darin, die Bandstruktur mit zwei verschiedenen Austausch-Korrelationsfunktionalen zu bestimmen und anschließend miteinander zu vergleichen. Zum einen kam das standard Funktional von Perdew-Burke-Enzerhof, als Vertreter für die Generalized-Gradient-Approximation, zum Einsatz. Zum anderen kam das Gaussian-Perdew-Burke-Enzerhof Funktional, als Vertreter der Hybrid-Funktionale, zum Einsatz. Wie in vielen anderen Arbeiten vorher auch schon gezeigt wurde, versagt ersteres bei der vorhersage der Bandlücke um den H-Punkt. Zweiteres führt zweifelsfrei zu Bandstrukturen und Bandlücken, die mit experimentellen Ergebnissen vereinbar sind und sollte für weitere Berechnungen verwendet werden. Wie in Experimenten, oder Berechnungen mit der "many-body pertubation theory" (GW Approximation) gezeigt wurde, konnte auch hier nachgewiesen werden, dass Tellur ein Halbleiter mit einer kleinen Bandlücke ist.

Abstract

In this thesis, ab-initio calculations of the band structure of trigonal tellurium are concerned. The open-source program Quantum ESPRESSO was used for this purpose. The methodological procedure consisted of determining the band structure with two different exchange-correlation functionals and then comparing them with each other. On the one hand, the standard functional of Perdew-Burke-Enzerhof was used as a representative of the generalised gradient approximation. On the other hand, the Gaussian-Perdew-Burke-Enzerhof functional was used as a representative of the hybrid functionals. As has been shown in many other works before, the former fails to predict the band gap around the H point. The latter undoubtedly leads to band structures and band gaps that are consistent with experimental results and should be used for further calculations. As shown in experiments or calculations with the many-body pertubation theory (GW approximation), it could also be proven here that tellurium is a semiconductor with a small band gap.

Contents

1 Introduction

In recent decades, great progress has been made within laser technology. Meanwhile, ultra-short laser pulses with a duration of a few femtoseconds can be generated, which carry a large amount of energy alongside them [1]. This has led to new fields of research and experiments.

Usually, the ions of a material are in an equilibrium position. By using an ultrashort laser pulse, the ions can be shifted from their equilibrium position to a new equilibrium position and then perform oscillations around their position there. At the same time, the laser pulse is accompanied by a time-dependent phonon excitation. This process is also called displacive excitation of coherent phonons in metals and semi-metals. Experimental evidence is obtained by measuring the oscillations of the optical reflectivity of the material using a pump pulse and a delayed probe pulse. There is an urgent need to theoretically describe such interactions of ultrashort laser pulses and matter and to make predictions about such types of interaction by means of suitable methods [2].

Due to the fact that tellurium (Te) exhibits the same laser pulse induced excitation of coherent phonons, it is used here as a representative case of study. In addition to this property, however, tellurium has a number of other characteristics that makes it attractive as a candidate for study. For example, it exhibits highly efficient thermoelectricity [3] or a pressure-dependent transition from the semiconducting phase to a metallic phase [4]. As a subject of investigation, it is therefore located primarily in experimental and computational solid-state physics, as well as in the material sciences.

The aim of the work is to improve the prediction of the band structure of tellurium by using a hybrid density functional theory (DFT) and to form a basis for further theoretical description of the above-mentioned interactions. Hybrid approximations to DFT are a mixture of the Hartree-Fock (HF) theory for the description of exact exchange and the DFT. For comparison, the band structure is also calculated with the conventional DFT, e.g. with the Perdew-Burke-Enzerhof (PBE) functional.

The thesis begins with a general introduction to the theoretical foundations of the DFT and its components. In the following third section, the research methods are discussed, as well as the details to be observed in the computer-based calculation on the basis of the DFT. Results are presented and evaluated in the fourth section. Finally, a short summary and a conclusion follow in the fifth section.

2 Theoretical Background

Behind every great discovery is a theory. In order to understand the essential aspects of the methods used in this work, a certain basic theoretical knowledge is also indispensable here. The crucial tool to describe interacting many-particle systems is provided in the following.

2.1 Hartree-Fock Equations

This section is intended to give a brief introduction to the Hartree-Fock equations, as they are generally essential for hybrid functionals.

The HF equations are an approximation to the solution of the many-body Schrödinger equation (SGE). The approximation is necessary because the SGE, as a partial differential equation, cannot be solved, except for the simplest systems. The main idea is to assume that the electrons interact, but that this interaction is so small that a solution in the form of the Slater determinant is possible [5]. Furthermore the usual Born-Oppenheimer approximation and the mean-field approximation are assumed. Relativistic effects are neglected.

V.Fock has shown in his article 'Näherungsmethode zur Lösung des quantenmechanischen Mehrkörperproblems' (1930) that Hartree's approximation method for determining the solution of the many-body problem is not accurate enough. He has established a system of equations for three-dimensional wave functions using the variational principle, which gives more accurate solutions than the mean-field approximation [6].

Without going into the derivation of the HF equations in more detail here, this one is about minimizing the energy $E = \langle \Psi | \hat{H} | \Psi \rangle$, where Ψ is a quantum state with the lowest energy, by varying the $\phi_i(\mathbf{r})$ and thereby satisfying the conditions (Orthogonality) [5]:

$$\frac{\delta E}{\delta \phi_i^*} = 0 \tag{1}$$

$$\int d\mathbf{r} \phi_i^*(\mathbf{r}) \phi_j(\mathbf{r}) = \delta_{ij} \tag{2}$$

Performing this calculus of variations then leads to the equations:

$$\left[-\frac{\nabla^2}{2} + V_n(\mathbf{r}) + V_H(\mathbf{r}) \right] \phi_i(\mathbf{r}) + \int d\mathbf{r}' V_X(\mathbf{r}, \mathbf{r}') \phi_i(\mathbf{r}') = \epsilon_i \phi_i(\mathbf{r}) \tag{3}$$

$$n(\mathbf{r}) = \sum_i |\phi_i(\mathbf{r})|^2 \tag{4}$$

$$\nabla^2 V_H(\mathbf{r}) = -4\pi n(\mathbf{r}) \tag{5}$$

The exact form of the Fock exchange potential V_X is given by the following expres-

sion:

$$V_X(\mathbf{r}, \mathbf{r}') = -\sum_j \frac{\phi_j^*(\mathbf{r}')\phi_j(\mathbf{r})}{|\mathbf{r} - \mathbf{r}'|} \tag{6}$$

The index j runs over the occupied single-particle states. This potential emerges because of the Pauli Principle. However, this additional potential is accompanied by an integration over the variable $\mathbf{r}'$, which makes the practical solution of the HF equations much more difficult [5].

2.2 Density Functional Theory

This section is now about the DFT. The basic concepts and ideas are presented and explained below. It is the tool for various calculations in solid state physics, chemistry or other areas in the natural sciences and is used in many programs nowadays.

2.2.1 Functionals

As the name 'Density **Functional** Theory' suggests, this theory has something to do with functionals. A short mathematical definition and its practical meaning is given hereafter.

Definition (compare [7])
Let $\mathbb{K} = \{\mathbb{R}, \mathbb{C}\}$, $V \in \mathbb{K}$ be a vector space and $f \in V$ a function. A functional Φ is a mapping from V into $\mathbb{K}$:

$$\Phi : f \mapsto \Phi[f] \in \mathbb{K}$$

In simple terms, this means that a functional takes as argument a function and returns a single value of that function. A simple example is the functional:

$$\Phi[f] = \int_{-1}^{1} f(x)dx \quad \text{with} \quad f(x) = x^2 + 1$$

which leads to $\Phi[f] = \frac{8}{3}$, which is a single value [8].

2.2.2 The Hohenberg-Kohn Theorem

An arbitrary system of interacting particles is considered, which is in an external potential $V_n(\mathbf{r})$. Fixed nuclei are assumed. From the given hamiltonian follow the two underlying theorems for the DFT.

Theorem I
For the system described above, the potential $V_n(\mathbf{r})$ results from the ground state density $n_0(\mathbf{r})$ and is uniquely determined except for one constant.

Corollary I
All characteristics of a system follow from the ground state density. This can be

concluded from the complete determinability (except for an energy shift) of the Hamiltonian and the wave functions.

Proof

Let $V_n^{I,II}(\mathbf{r})$ be two different potentials from which the same ground state density $n(\mathbf{r})$ follows. These potentials are accompanied by two different Hamiltonians $\hat{H}^{I,II}$ and two ground-state wave functions $\psi^{I,II}$ which are assumed to should have the same ground-state density $n_0(\mathbf{r})$. Furthermore, the Dirac notation for the expectation value is introduced as follows:

$$E = \langle \psi | \hat{H} | \psi \rangle = \int d\mathbf{r}_1 \cdots d\mathbf{r}_N \ \psi^*(\mathbf{r}_1, \cdots, \mathbf{r}_N) \hat{H} \psi(\mathbf{r}_1, \cdots, \mathbf{r}_N) \tag{7}$$

It is obvious that ψ^I is not the ground state of $\hat{H}^{II}$ and that ψ^{II} is not the ground state of $\hat{H}^I$. Accordingly, it follows for the energies:

$$E^I = \langle \psi^I | \hat{H}^I | \psi^I \rangle < \langle \psi^{II} | \hat{H}^I | \psi^{II} \rangle \tag{8}$$

$$E^{II} = \langle \psi^{II} | \hat{H}^{II} | \psi^{II} \rangle < \langle \psi^I | \hat{H}^{II} | \psi^I \rangle \tag{9}$$

The right terms on both equations can be rewritten:

$$\langle \psi^I | \hat{H}^{II} | \psi^I \rangle = \langle \psi^I | \hat{H}^I | \psi^I \rangle + \langle \psi^I | \hat{H}^{II} - \hat{H}^I | \psi^I \rangle \tag{10}$$

$$\langle \psi^{II} | \hat{H}^I | \psi^{II} \rangle = \langle \psi^{II} | \hat{H}^{II} | \psi^{II} \rangle + \langle \psi^{II} | \hat{H}^I - \hat{H}^{II} | \psi^{II} \rangle \tag{11}$$

The definitions of the energy and the hamiltonians leads to:

$$\langle \psi^I | \hat{H}^{II} | \psi^I \rangle = E^I + \int n_0(\mathbf{r}) \left[V_n^{II}(\mathbf{r}) - V_n^I(\mathbf{r}) \right] d\mathbf{r} \tag{12}$$

$$\langle \psi^{II} | \hat{H}^I | \psi^{II} \rangle = E^{II} + \int n_0(\mathbf{r}) \left[V_n^I(\mathbf{r}) - V_n^{II}(\mathbf{r}) \right] d\mathbf{r} \tag{13}$$

Accordingly, this follows from equations (8) and (9):

$$E^I < E^{II} + \int n_0(\mathbf{r}) \left[V_n^I(\mathbf{r}) - V_n^{II}(\mathbf{r}) \right] d\mathbf{r} \tag{14}$$

$$E^{II} < E^I + \int n_0(\mathbf{r}) \left[V_n^{II}(\mathbf{r}) - V_n^I(\mathbf{r}) \right] d\mathbf{r} \tag{15}$$

Addition of these two equations leads to the opposite statement $E^I + E^{II} < E^I + E^{II}$. This means that there are no two potentials which differ in more than one constant leading to the same non-degenerate ground state density. It is to be mentioned that at the beginning of the proof with the strict inequality of (8) and (9) it was assumed that the ground state is not degenerate. In the original proof of W. Kohn [9] the same was assumed. An argument for the correctness of corrolary I is, that the ground-state density uniquely determines the hamiltonian. Therefore all wave

functions are determined by solving the SGE with this hamiltonian.

Theorem II

In addition, the energy is given as a density dependent functional $E[n]$, valid for each potential $V_n(\mathbf{r})$, which reflects the ground state energy in the point of global minimum. Moreover, the density $n(\mathbf{r})$, which minimizes the energy functional, is the exact ground state density $n_0(\mathbf{r})$ of the system.

Corrollary II

The determination of the ground state density and the ground state energy follows from the energy functional.

Proof

Hohenberg and Kohn have confined the proof of the second theorem to densities $n(\mathbf{r})$ which are ground state densities of the electron hamilatonian with a potential $V_n(\mathbf{r})$. Due to the properties, these densities are also called V-representable. Within these "space", the densities can be defined as functionals. Due to theorem I and corrolary II, any quantity that enters the energy functional can be considered a density functional. So, it follows:

$$E_{HK}[n] = F_{HK}[n] + E_{II} + \int V_n(\mathbf{r})n(\mathbf{r})d\mathbf{r} \qquad (16)$$

Here E_{II} is the interaction energy of the nuclei and F_{HK} is a functional which includes internal, kinetic and potential energy of the electron system.

Let $n^I(\mathbf{r})$ be the ground-state density with a potential $V_n^I(\mathbf{r})$ and $\psi^I(\mathbf{r})$ the wave function of the unique ground-state. It follows:

$$E^I = E_{HK}[n^I] = \langle \psi^I | H^I | \psi^I \rangle \qquad (17)$$

Now another density $n^{II}(\mathbf{r})$ and another wave function $\psi^{II}(\mathbf{r})$ is given, which is obviously not the ground state. Following from this, the energy E^{II} must be greater then E^I:

$$E^I = \langle \psi^I | H^I | \psi^I \rangle \; < \; \langle \psi^{II} | H^I | \psi^{II} \rangle = E^{II} \qquad (18)$$

This means that if you calculate the energy functional for the ground state density it is in any case smaller than for any other density functionals. Furthermore, the exact ground-state density and the ground-state energy follow from the minimization of the total energy by the variation of the density with known functional $F_{HK}[n]$. This gives rise to corollary II.

Besides the theorems presented here, there are extensions, such as spin DFT or time-dependent DFT. In the former, for example, a spin density $s(\mathbf{r})$ is introduced in addition to the particle density, so that for the functional $E = E_{HK}[n, s]$ is valid.
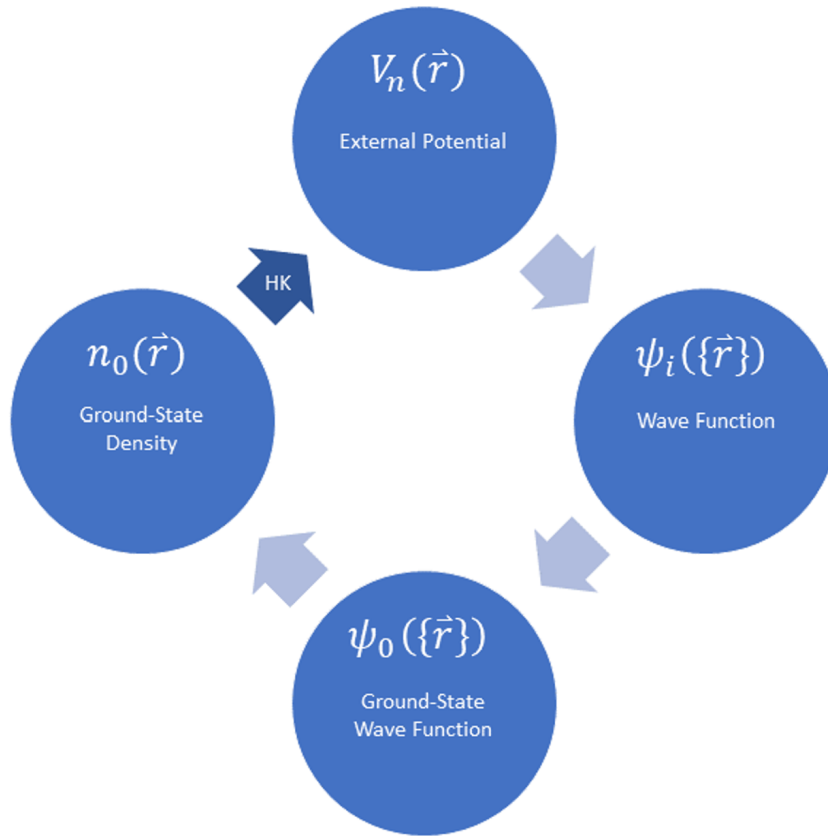
Figure 1: Hohenberg-Kohn Theorem: The arrows, which are less transparent, are intended to represent the conventional solutions of the SGE. The external potential V_n determines the solutions of the system. Via the Hohenberg-Kohn theorem, the ground state density n_0 is linked to the external potential V_n.

2.2.3 The Kohn-Sham Theorem

This section from the theory part is devoted to the Kohn-Sham theorem. It is one of the most basic concept for the calculation of electronic structures nowadays. In summary, it is about *'to replace the original many-body problem by an auxiliary independet-particle problem.'*([10],p.145). This replaced system is more easy to handle. More precisely, the theorem makes the assumption that the ground state density of the system under consideration is equal to the ground state density for a chosen non-interacting system. For this system, equations arise which can be solved numerically and whose nontrivial many-body terms are unified in an exchange-correlation (xc) functional of the density. Thus, the solutions of these equations lead to the ground state density and the energy of the original system, where the precision is determined by the xc functional [10].

Besides the first assumption that the ground state density can be represented by that of an auxiliary system (noninteracting-V-representability), it is further assumed that the Hamiltonian for this system is in the form of single-particles. Here, however, a local potential $V_{eff}^{\sigma}(\mathbf{r})$ is introduced, which acts on an electron with spin σ at the

point $\mathbf{r}$. The Hamiltonian is then given by:

$$\hat{H}_{aux}^{\sigma} = -\frac{1}{2}\nabla^2 + V^{\sigma}(\mathbf{r}) \tag{19}$$

In total, there are $N^{\sigma} = N^{\uparrow} + N^{\downarrow}$ independent electrons in the system, one of which has spin-up and the other spin-down. In the lowest-energy state, i.e. in the ground state, the Hamiltonian has eigenfunctions $\psi_i^{\sigma}(\mathbf{r})$ and the eigenvalues ϵ_i^{σ}. Therefore the density is given by:

$$n(\mathbf{r}) = \sum_{\sigma} n(\mathbf{r}, \sigma) = \sum_{\sigma} \sum_{i=1}^{N^{\sigma}} |\psi_i^{\sigma}(\mathbf{r})|^2 \tag{20}$$

The kinetic energy T_s of the independent particles is given by:

$$T_s = -\frac{1}{2} \sum_{\sigma} \sum_{i=1}^{N^{\sigma}} \langle \psi_i^{\sigma} | \nabla^2 | \psi_i^{\sigma} \rangle = \frac{1}{2} \sum_{\sigma} \sum_{i=1}^{N^{\sigma}} \int |\nabla \psi_i^{\sigma}(\mathbf{r})|^2 \, d\mathbf{r} \tag{21}$$

At last the Hartree energy is given by following expression (represents the coulomb interaction of the density with itself):

$$E_H[n] = \frac{1}{2} \int \frac{n(\mathbf{r})n(\mathbf{r}')}{|\mathbf{r} - \mathbf{r}'|} \, d\mathbf{r}d\mathbf{r}' \tag{22}$$

Rewriting the Hohenberg-Kohn theorem leads to the Kohn-Sham equation for the energy:

$$E_{KS} = T_s[n] + \int V_n(\mathbf{r})n(\mathbf{r}) \, d\mathbf{r} + E_H[n] + E_{II} + E_{xc}[n] \tag{23}$$

As may be seen, the first three terms in this equation are equivalent to the terms of the independent electron approximation. In addition, there is the energy term for the interaction of the nuclei and the xc functional. Comparing the second theorem of Hohenberg-Kohn with the expression of the Kohn-Sham equation, an expression for the xc functional can be given:

$$E_{xc}[n] = F_{HK}[n] - (T_s[n] + E_H[n]) \tag{24}$$

It's obvious that E_{xc} has to be a functional, because all the terms on the right side are functionals. Furthermore $n(\sigma, \mathbf{r})$ is spin- and position dependent [10].

2.2.4   Solution of the Kohn-Sham Auxiliary System

To solve the auxiliary system, and ultimately to find a solution for the original system, the variational principle and the method of lagrange multipliers are used. It is therefore a minimization problem.

The expression for E_{KS} from equation (23) is the starting point. When deriving to

$\psi_i^{\sigma*}$, the chain rule is applied, which then leads to the following expression:

$$\frac{\delta E_{KS}}{\delta \psi_i^{\sigma*}(\mathbf{r})} = \frac{\delta T_s}{\delta \psi_i^{\sigma*}(\mathbf{r})} + \left[\frac{E_n}{\delta n(\mathbf{r}, \sigma)} + \frac{E_{Hartree}}{\delta n(\mathbf{r}, \sigma)} + \frac{E_{xc}}{\delta n(\mathbf{r}, \sigma)} \right] \frac{\delta n(\mathbf{r}, \sigma)}{\delta \psi_i^{\sigma*}(\mathbf{r})} = 0 \qquad (25)$$

Note that E_n is corresponding to the term $\int V_n(\mathbf{r})n(\mathbf{r})d\mathbf{r}$ of equation (23). Besides, the orthonormalization condition $\langle \psi_i^\sigma | \psi_j^{\sigma'} \rangle = \delta_{i,j}\delta_{\sigma,\sigma'}$ must be fulfilled. Thus, the problem at hand can be viewed equivalently as the derivation of the SGE from Rayleigh-Ritz's principle ($\Omega_{RR} = \langle \Psi | \hat{H} - E | \Psi \rangle$). Now it makes sense to use the respective definitions from above for T_s and $n^\sigma(\mathbf{r})$ and derive them and use the lagrange multipliers to handle the constraints:

$$\frac{\delta T_s}{\delta \psi_i^{\sigma*}(\mathbf{r})} = -\frac{1}{2}\nabla^2 \psi_i^\sigma(\mathbf{r}) \qquad (26)$$

$$\frac{\delta n^\sigma(\mathbf{r})}{\delta \psi_i^{\sigma*}(\mathbf{r})} = \psi_i^\sigma(\mathbf{r}) \qquad (27)$$

This then leads to an expression which resembles the SGE:

$$H_{KS}^\sigma \psi_i^\sigma(\mathbf{r}) = \epsilon_i^\sigma \psi_i^\sigma \qquad (28)$$

Here is:

$$H_{KS}^\sigma(\mathbf{r}) = -\frac{1}{2}\nabla^2 + V_{KS}^\sigma(\mathbf{r}) \qquad (29)$$

$$V_{KS}^\sigma(\mathbf{r}) = V_n(\mathbf{r}) + \frac{\delta E_H}{\delta n(\mathbf{r}, \sigma)} + \frac{\delta E_{xc}}{\delta n(\mathbf{r}, \sigma)} = V_n(\mathbf{r}) + V_H(\mathbf{r}) + V_{xc}^\sigma(\mathbf{r}) \qquad (30)$$

The last three equations are the well-known expressions of the Kohn-Sham theorem. The equations correspond to those of independent particles . The potential which results from the resulting density must be found self-consistently (see next section). However, in order to find the exact ground state density, an expression for the xc functional must be given, which turns out to be not too easy. Exact solutions do not exist for this functional, but there are good approximations which lead to general valid results (see next but one section).

2.2.5 Self-Consistent Solution

The exact way to achieve a self-cosistent solution of the Kohn-sham states is shown in Fig. 2. Essentially, it is a matter of calculating the Kohn-Sham equations under the condition of consistency of potential and density. Thus, to achieve self-consistency, the potential and the density are successively changed. It is an iterative solution process, which can be represented as follows:

$$V_i \rightarrow n_i \rightarrow V_{i+1} \rightarrow n_{i+1} \rightarrow \cdots$$
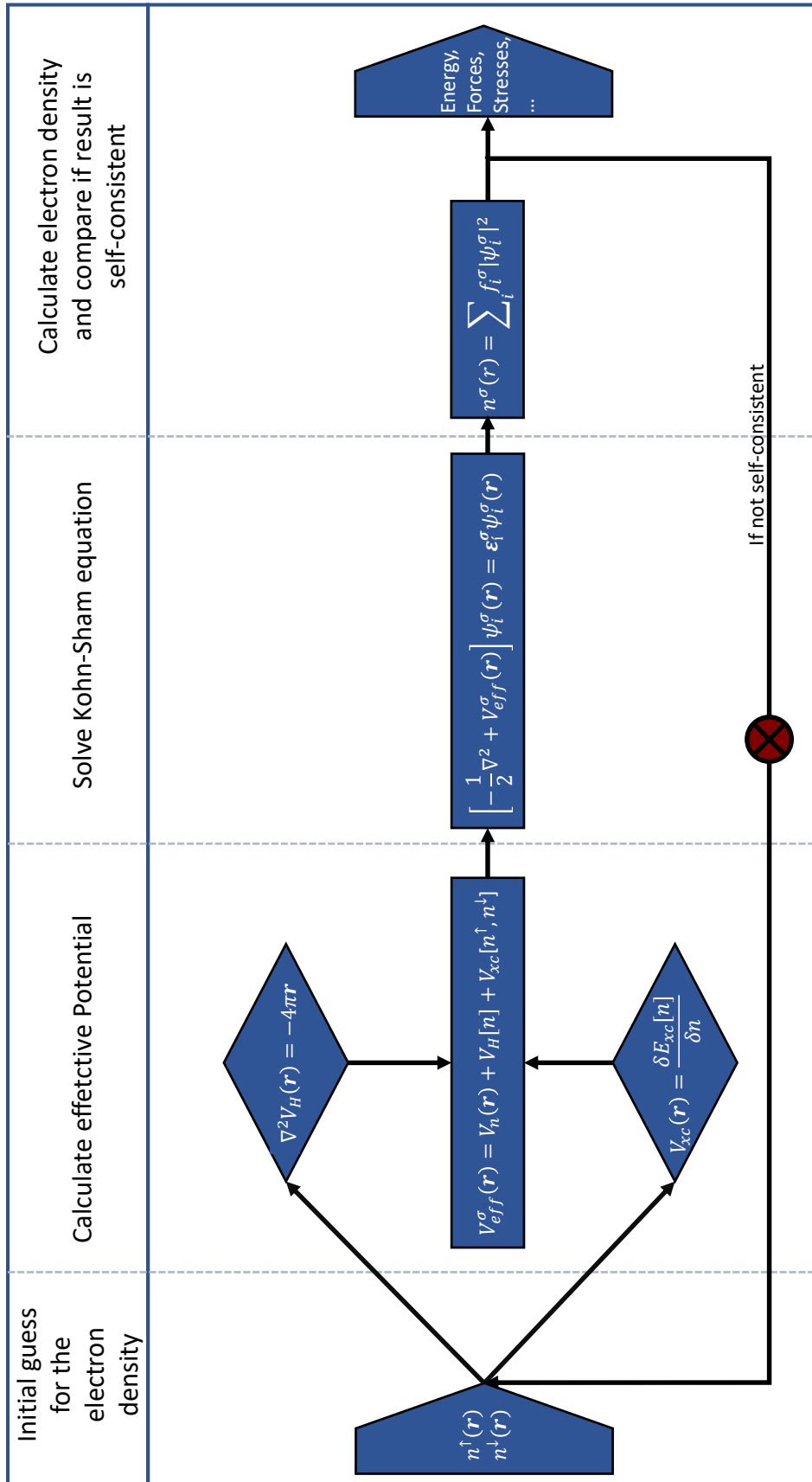
Figure 2: Self-Consistent Solution of the Kohn-Sham Equations

It should be noted that the potential unique to the ground state density is at a minimum that of the Kohn-Sham potential $V_{eff}^{\sigma}(\mathbf{r})|_{min} = V_{KS}^{\sigma}(\mathbf{r})$ (Hohenberg-Kohn Theorem). Therefore the symbol V_{eff}^{σ} in Fig. 2. Further it would be more exact, but also clearly more complicated, if the xc functional is defined as a functional of the spin density matrix. Thus the Kohn-Sham Hamiltonian would be a 2x2 matrix and harder to solve. Due to this fact, the expression for the electron density in Fig. 2. Finally, for spin-polarized systems, two calculations have to be performed simultaneously, each for one of the two spin directions.

2.2.6 Exchange-Correlation Functionals

As mentioned before, xc functionals play a major role in the computation of electronic structures by means of the Kohn-Sham theorem. In the meantime, a large number of such functionals exist. Two of the most frequently used functionals are the Local Density Approximation (LDA) and the Generalized-Gradient Approximations (GGA), which are also discussed in this chapter.

LDA
The LDA is a comparatively simple approximation for the xc functional. As the name suggests, it is a local functional whose xc energy density is the same as for a homogeneous electron gas and depends only on the position $\mathbf{r}$. The expression for the functional is as follows:

$$E_{xc}^{LSDA}[n^{\uparrow}, n^{\downarrow}] = \int n(\mathbf{r})\epsilon_{xc}^{hom}(n^{\uparrow}(\mathbf{r}), n^{\downarrow}(\mathbf{r}))d\mathbf{r} \tag{31}$$

$$= \int n(\mathbf{r})\left[\epsilon_{x}^{hom}(n^{\uparrow}(\mathbf{r}), n^{\downarrow}(\mathbf{r})) + \epsilon_{c}^{hom}(n^{\uparrow}(\mathbf{r}), n^{\downarrow}(\mathbf{r}))\right]d\mathbf{r}$$

An analytical expression exists for the exchange energy of the homogeneous electron gas. The correlation energy could be calculated by Monte Carlo methods. Due to the simplicity of this type of functional, the computational cost is still relatively low.

GGA's
For many molecules and solids, GGA's are the first choice to get good results. Compared to the previously mentioned LDA, GGA's are semilocal. This is because the xc energy density now also depends on the gradient of the electron density. In simple words, this means that not only the exact location $\mathbf{r}$ is crucial, but also a small region around this location. The mathematical expression then looks as follows:

$$E_{XC}^{GGA}[n^{\uparrow}, n^{\downarrow}] = \int n(\mathbf{r})\epsilon_{XC}(n^{\uparrow}, n^{\downarrow}, |\nabla n^{\uparrow}|, |\nabla n^{\downarrow}|, ...)d\mathbf{r} \tag{32}$$

$$= \int n(\mathbf{r})\epsilon_{x}^{hom}(n) \, F_{XC}(n^{\uparrow}, n^{\downarrow}, |\nabla n^{\uparrow}|, |\nabla n^{\downarrow}|, ...)d\mathbf{r}$$

ϵ_{x}^{hom} corresponds to the exchange energy of an unpolarized electron gas and F_{xc} is

dimensionless, but depends on the density and the density gradient. Many types of such GGA's exist, differing essentially in the expression F_{xc}.
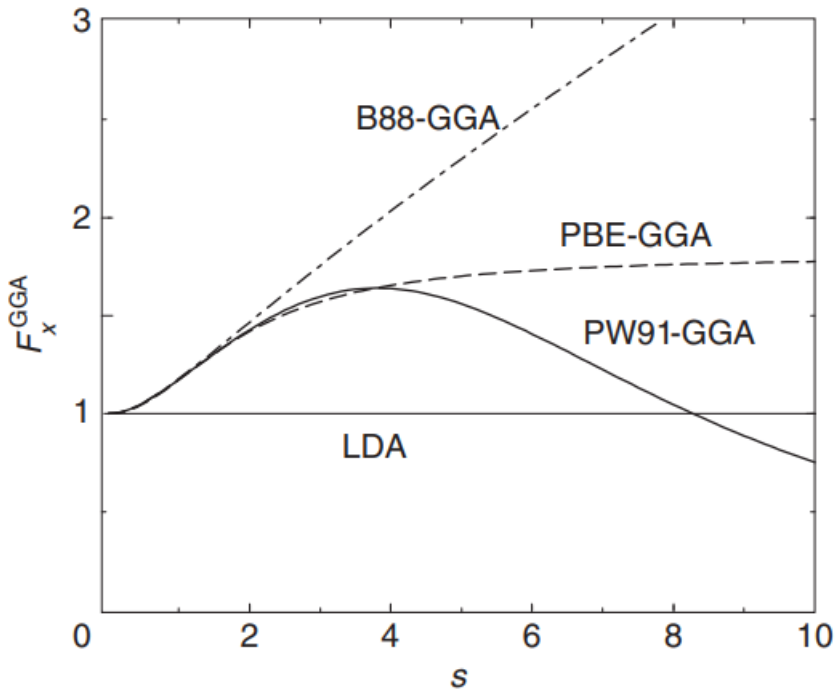

Figure 3: Comparison of different types of GGA's ([10],p.181)

In Fig. 3, for example, the exchange factor F_x is plotted against the density gradient s. Without going into more detail, this can be defined for the m-th order as follows:

$$s_m = \frac{|\nabla^m n|}{(2k_F)^m n} \tag{33}$$

Where k_F is the Fermi-momentum. s basically indicates how fast the density changes in units of the Fermi momentum. What is interesting about this Figure is that it can be seen that the different functionals in the small range $s < 3$ all have a similar appearance and thus give similar physical results in this range (for many standardized systems). In the larger gradient range the functionals then do differ considerably, but this range alone is not so strongly relevant for the physical evaluation. The improvement of GGA's is, the fact that $F_x \geqslant 1$ and therefore leads to a smaller exchange energy and a correction of the overestimated LDA overbinding. It is also possible to specify an expression for F_c. Typically, however, the correlation term is smaller than the exchange term. Due to an additional dependence of the xc energy density, the calculations with GGA's are more complex.

In this work, the PBE functional, which can also be seen in Fig. 3, is used for some calculations. Without going into the exact appearance of F_x and F_c [11], this functional provides good resulsts in many applications [12], even if the functional is non-empirical.

Hybrid Functionals

Finally, something about hybrid functionals. As the name 'hybrid' suggests, they are a combination of the DFT and HF. This can be illustrated by an example: While LDA and GGA's mostly underestimate the band gap, the HF theory mostly overestimates it. In order to find a consensus, one could conclude that a combination of both is useful to get a result which agrees with the experiment. For the representation of the ratios a factor α is introduced and additionally there is the HF term in the representation for the xc functional:

$$E_{xc}^{hyb} = \alpha E_x^{HF} + (1 - \alpha)E_x^{GGA} + E_c^{GGA} \tag{34}$$

This means that for $\alpha = 0$ the 'normal' xc functional is present, whereas for the other extremal case $\alpha = 1$ only the HF exchange is taken into account.

The PBE0 functional can be cited as an example. Here, the mixing parameter $\alpha = 0.25$. Thus, it follows:

$$E_{xc}^{PBE0} = \frac{1}{4}E_x^{HF} + (1 - \frac{1}{4})E_x^{PBE} + E_c^{PBE} = E_{xc}^{PBE} + \frac{1}{4}(E_x^{HF} - E_x^{PBE}) \tag{35}$$

In this work, in addition to the PBE-GGA functional, the Gau-PBE functional is also used, which belongs to the hybrid functionals. 'Gau' is an abbreviation for Gaussian. In the following it is briefly explained how the Gau-PBE is composed and what its advantages are. An idea that is also used in the Heyd-Scuseria-Ernzerhof (HSE) functional, for example, is the range subdivision. The HF exchange energy is divided into short and long range contributions to the Coulomb interaction. In other words, the electron repulsion operator $\frac{1}{r}$ is split into an HF term and a DFT term and looks like this:

$$\frac{1}{r} = \left(\frac{1}{r} - O\right)_{DFT} + O \tag{36}$$

Where O is an expression for the modified HF exchange term. The Gau-PBE now uses a gaussian function for the modified HF term:

$$O = \beta e^{-\tilde{\alpha} r^2} \tag{37}$$

The parameters are determined as follows: $\beta = 0.24$, $\tilde{\alpha} = 0.15$. This hybrid Scheme is used in conjunction with the PBE-GGA Functional [13]. The accuracy of the functional is comparable to longer established functionals, such as HSE, but the advantage is in the computation time. As song and hirao have shown in their paper, the computation time for the first SCF cycle is at least twice as fast as that of the hybrid functional HSE [13]. Nevertheless, it is still about two and a half times as long as that of the PBE-GGA functional.

In summary, the functionals are shown in Fig. 4. With increasing height, the complexity of the calculations increases, but also the accuracy of the calculations. One should always keep in mind the system to be calculated, then the choice of the xc

functional stands and falls with it. The groups of xc functionals, which are used in this paper are marked with a circle.
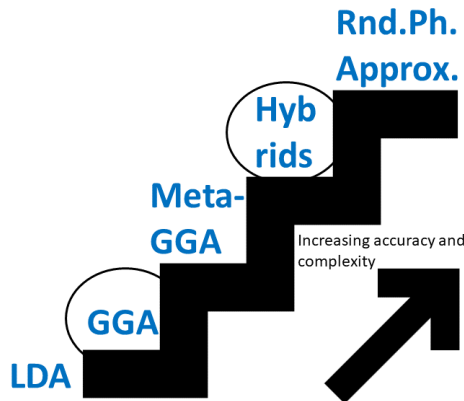

Figure 4: Visualization of the different xc Functionals

2.3 Spin-Orbit Coupling

The last section in this chapter is about the Spin-Orbit coupling (SOC). As we will see later it can have an decisive influence on the band structure.

The phenomenon of SOC is relatively easy to describe using the Bohr model of the atom: An electron has a magnetic moment due to the intrinsic angular momentum (spin). This electron orbits around the positively charged atomic nucleus which is accompanied by an angular momentum. In the rest system of the electron, the nucleus slowly orbits around the electron and due to the charge, this motion generates a circular current, which according to the law of Biot-Savart generates a magnetic field, parallel to the angular momentum vector. This magnetic field now interacts with the spin induced magnetic momentum of the electron.

Considering a solid, the spin-orbit coupling just described can cause a cancellation of the degeneracy of the $\psi_{\mathbf{k}}(\mathbf{r}, \uparrow)$ and $\psi_{\mathbf{k}}(\mathbf{r}, \downarrow)$ states. It should be noted, however, that Kramer's degeneracy must be preserved between the $\psi_{\mathbf{k}}(\mathbf{r}, \uparrow)$ and $\psi_{\mathbf{k}}^*(\mathbf{r}, \downarrow)$ states. This is, as already described above, a consequence of the fundamental time reversal invariance. The state $\psi_{\mathbf{k}}^*(\mathbf{r}, \downarrow)$ is the conjugate complex wave function where both the spin and the wave vector of the electron are reversed. For spinless particles just the relation results $E_n(\mathbf{k}) = E_n(-\mathbf{k})$ [14].

If inversion symmetry is present in a crystal, SOC does not cause separation of non-degenerate states with opposite spin. This is because the state $\psi_{\mathbf{k}}(\mathbf{r})$ is energetically equivalent to the state $\psi_{\mathbf{k}}(-\mathbf{r})$ due to the symmetry. Thus, Kramer's degeneracy holds.

It may be that degenerate states exist at certain points in the Brillouin Zone (BZ) and SOC can play out its effects there. As an example, a point with cubic symmetry is assumed, which sits in the center of the BZ. The p-bands are considered, which are built up from the states $p_{x,y,z}$ of the atom. Without SOC, there is a 6-fold degeneracy at $\mathbf{k} = 0$, since each p state can accept 2 electrons with opposite spin

(compare Figure 5a). If the SOC now acts, a splitting into a fourfold and a twofold degenerate level at $\mathbf{k} = 0$ results if inversion symmetry is present (Figure 5b). If there is no inversion symmetry, the Kramers degeneracy is cancelled Figure 5c) [14].
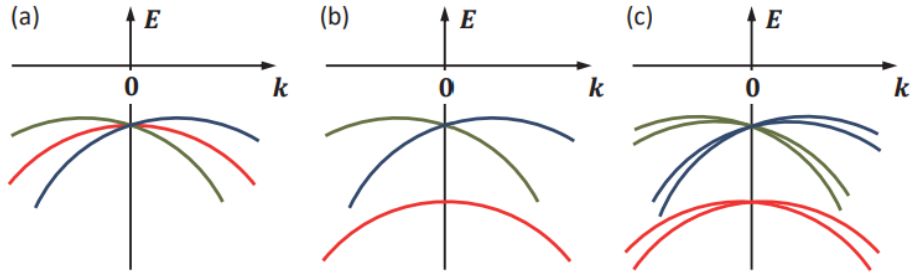

Figure 5: Influence of the SOC on the band structure([14],p.344)

3 Research Method

In practice, calculations based on the DFT are performed with a computer. Based on the theory introduced in section two, the calculations are performed using the program Quantum ESPRESSO (QE). In the following, a small overview of the basics of this program and the practical use of the DFT is given.

3.1 Pseudopotentials

Pseudopotentials are an approximation for the actual potential present. In principle, they emulate the real potential. The main idea of this method is to categorize the electrons of an atom into two classes: the core electrons and the valence electrons. On the one hand, the core electrons are so strongly bound and so strongly localized in the inner closed shells that they remain essentially unchanged. Basically, it does not matter for the core electrons whether the atom is a part of a solid or whether it is free. On the other hand, the valence electrons, which are present in the outer filled or unfilled shells, are responsible for bonding, ionization or other activities. To reduce the computational effort, the frozen core approximation now assumes that the charge of the core is reduced by the amount of the core electrons. The status quo is now a new nucleus with reduced charge, which has a smaller influence on the valence electrons (compare Fig. 6) [15].
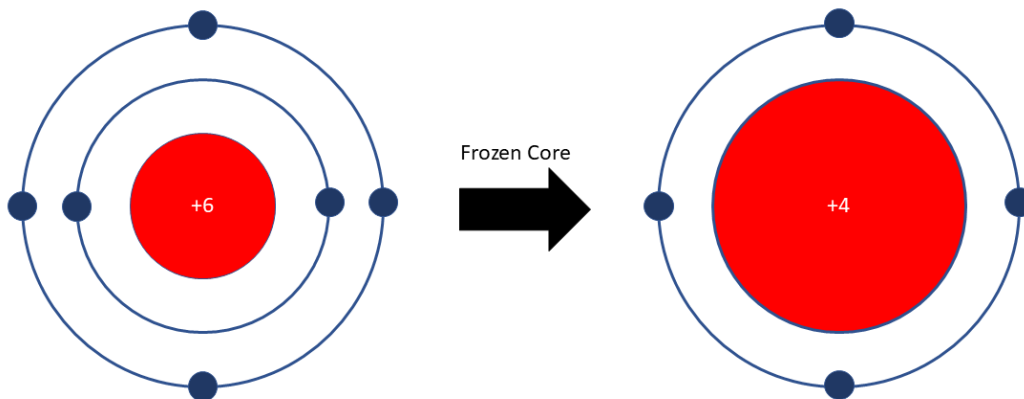

Figure 6: Simplified illustration of the frozen core approximation

An example which is a bit more impressive is platinum. This element has a total of 78 electrons, 10 of which are valence electrons. The application of the frozen nucleus approximation would already bring a considerable advantage in the calculation, since the computational load would be reduced by more than one third (compared to Fig. 6) [15].

Usually, wavefunctions oscillates when they are near highly localized core regions. This is based on the fact that they want to be orthogonal to the core states (orthogonality ensures that each wave function is independent and unique and thus obeys the

Pauli principle). The problem with this type of wave function is that it is difficult to describe, let alone compute. The advantage of the frozen core approximation is that when creating pseudopotentials, the wavefunction itself, as well as the pseudopotential in the core region, can be softened [15]. The situation is shown schematically in Fig. 7. The all-electron wave function Ψ_{AE} wiggles near the core region whereas the pseudized wave function Ψ_{PP} is softened. The same yields for the all-electron potential U_{AE} and the pseudopotential U_{PP}.
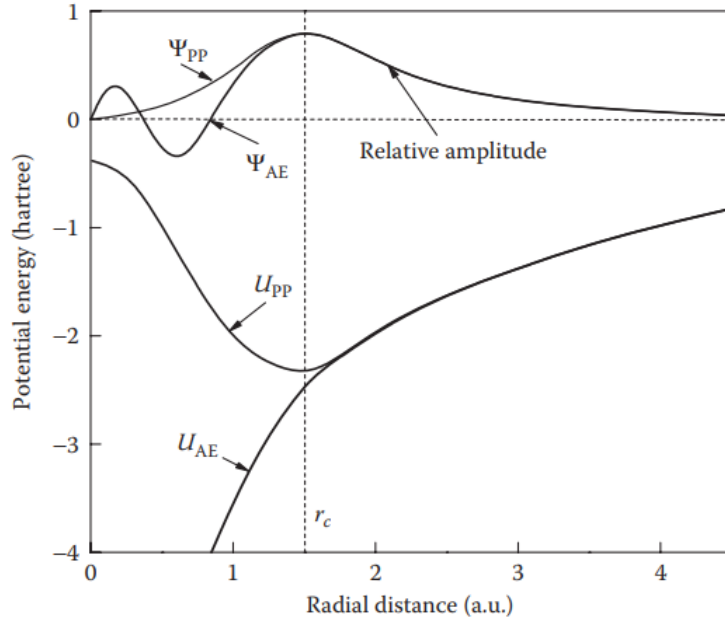
Figure 7: Pseudized 3s wave function as well as belonging potentials ([15],p.177)

The usage of Pseudopotentials leads to following advantages [15]:

1. less plane waves (see next section) needed, which leads to a faster calculation

2. a change of energy is more likely with pseudopotentials, because a large part of the not changing energy is excluded by the frozen core approximation from the beginning.

3. errors due to pseudopotentials relatively low

There are essentially three groups of pseudopotentials, all of which certainly have their reason for being. On the one hand, there are Norm-Conseving Pseudopotentials (NCPPs), on the other hand Ultrasoft Pseudopotentials (USPPs) and Projector augemted waves (PAW). In this work, the former are used for the calculations. In these, it is assumed that the norm of the pseudized wave function corresponds to that of the all-electron wave function (up to a core-radius r_c)[15]:

$$\int_0^{r_c} |\Psi_{AE}|^2 \, d\mathbf{r} = \int_0^{r_c} |\Psi_{PP}|^2 \, d\mathbf{r} \tag{38}$$

16

More precisely, an SG15 Optimized Norm-Conserving Vanderbilt (ONCV) pseudopotential was chosen for the calculation. This was created using the ONCVPSP code, which is based on the work of D.R. Hamann [16]. The crucial parameters of the pseudopotential were optimized in such a way that they correspond with high accuracy to the results of the calculations with all-electrons [17]. Furthermore, a fully relativistic SG15 ONCV pseudopotential was chosen so that calculations with SOC can be performed. These were generated by P. Scherpelz et al. [18].

It is worth mentioning that this pseudopotential was chosen because of repeated calculation errors with pseudopotentials of class PAW and USPP, especially with respect to hybrid functionals. Furthermore, at the moment there are no pseudopotentials that are specific for hybrid functionals or non-local functionls [19].

3.2 Plane Waves

As mentioned above, QE uses a plane wave basis set to calculate the solution of the Kohn-Sham states. Hence the name of the module PWscf (Plane-Wave Self-Consistent-Field), which is used for most of the calculations here. To put it in simple terms, the key concept in solving differential equations such as the SGE or the Kohn-Sham equation lies in the representation of these equations in a plane wave basis, respectively in the use of Fast-Fourier transform (FFT) [10].

A periodic wave function $\psi_i(\mathbf{r})$ can be represented in a complete set of Fourier components:

$$\psi_i(\mathbf{r}) = \sum_{\mathbf{q}} c_{i,\mathbf{q}} \frac{1}{\sqrt{\Omega}} e^{i\mathbf{q}\cdot\mathbf{r}} = \sum_{\mathbf{q}} c_{i,\mathbf{q}} |\mathbf{q}\rangle \tag{39}$$

Here $c_{i,\mathbf{q}}$ are the expansion coefficients and Ω is the volume of a solid. The plane waves $|\mathbf{q}\rangle$ obeying the orthonormalization condition, since:

$$\langle \mathbf{q}'|\mathbf{q}\rangle = \frac{1}{\Omega} \int_{\Omega} e^{-i\mathbf{q}'\cdot\mathbf{r}} e^{i\mathbf{q}\cdot\mathbf{r}} \, d\mathbf{r} = \delta_{\mathbf{q},\mathbf{q}'} \tag{40}$$

The wave approach in Fourier components can now be used in an equation similar to SGE:

$$\sum_{\mathbf{q}} \langle \mathbf{q}'|\hat{H}|\mathbf{q}\rangle c_{i,\mathbf{q}} = \epsilon_i \sum_{\mathbf{q}} \langle \mathbf{q}'|\mathbf{q}\rangle c_{i,\mathbf{q}} = \epsilon_i c_{i,\mathbf{q}'} \tag{41}$$

This is the representation of the SGE in the Fourier space. For a crystal whose potential V is periodic, a representation in Fourier components can also be made.

$$V(\mathbf{r}) = \sum_{m} V(\mathbf{G_m}) e^{i\mathbf{G}_m\cdot\mathbf{r}} \tag{42}$$

Here $V(\mathbf{G}_m)$ is defined as:

$$V(\mathbf{G}) = \frac{1}{\Omega_{\text{cell}}} \int_{\Omega_{\text{cell}}} V(\mathbf{r}) e^{-i\mathbf{G}\cdot\mathbf{r}} \, d\mathbf{r} \tag{43}$$

and Ω_{cell} is the voume of the primitive cell. The matrix elements are therefore:

$$\langle \mathbf{q}'|V|\mathbf{q}\rangle = \sum_m V(\mathbf{G}_m)\delta_{\mathbf{q}'-\mathbf{q},\mathbf{G}_m} \tag{44}$$

They are not zero, if $\mathbf{q}$ and $\mathbf{q}'$ differ by $\mathbf{G}_m$. One can now define $\mathbf{q} = \mathbf{k} + \mathbf{G}_m$ and $\mathbf{q}' = \mathbf{k} + \mathbf{G}_{m'}$, which differ by $\mathbf{G}_{m''} = \mathbf{G}_m - \mathbf{G}_{m'}$. Thus, the SGE in fourier space is given by:

$$\sum_{m'} H_{m,m'}(\mathbf{k})c_{i,m'}(\mathbf{k}) = \epsilon_i(\mathbf{k})c_{i,m}(\mathbf{k}) \tag{45}$$

Whereby the Hamiltonian is then also given in matrix representation:

$$H_{m,m'}(\mathbf{k}) = \langle \mathbf{k} + \mathbf{G}_m|\hat{H}|\mathbf{k} + \mathbf{G}_{m'}\rangle \tag{46}$$

$$= \frac{\hbar^2}{2m_e}|\mathbf{k} + \mathbf{G}_m|^2\delta_{m,m'} + V(\mathbf{G}_m - \mathbf{G}_{m'})$$

Similarly, the derivation of the Kohn-Sham equations in the Fourier space works in the same way. With this representation, computer-aided calculations can be performed.

Two things are worth mentioning here: First, $\mathbf{q}$ can be constrained in equation (39) such that $\mathbf{q} = \mathbf{k} + \mathbf{G}_m$. Thus, it follows:

$$\psi_{i,\mathbf{k}}(\mathbf{r}) = \sum_m c_{i,m}(\mathbf{k}) \times \frac{1}{\sqrt{\Omega}}e^{i(\mathbf{k}+\mathbf{G}_m)\cdot\mathbf{r}} = e^{i\mathbf{k}\cdot\mathbf{r}}\frac{1}{\sqrt{N_{\text{cell}}}}u_{i,\mathbf{k}}(\mathbf{r}) \tag{47}$$

Here Ω is $\Omega = N_{\text{cell}}\Omega_{\text{cell}}$ and $u_{i,\mathbf{k}}$ is:

$$u_{i,\mathbf{k}}(\mathbf{k}) = \frac{1}{\sqrt{\Omega_{\text{cell}}}}\sum_m c_{i,m}(\mathbf{k})e^{i\mathbf{G}_m\cdot\mathbf{r}} \tag{48}$$

As one might may see is this the Bloch theorem from classcial Solid-State physics. Furthermore follows:

$$\frac{1}{\Omega_{Cell}}\int_{Cell} u_{i,\mathbf{k}}^*(\mathbf{r}) \cdot u_{i',\mathbf{k}}(\mathbf{r}) \, d\mathbf{r} = \sum_m c_{i,m}^*(\mathbf{k})c_{i',m}(\mathbf{k}) = \delta_{i,i'} \tag{49}$$

This means that $c_{i,m}(\mathbf{k})$ are orthonormal vectors (in the index m). Second, one can find a set of eigenstates labeled $i = 1, 2, \cdots$ for each $\mathbf{k}$ by diagonalizing the hamiltonian in the basis of fourier components [10].

The plane wave basis is now the fundament to perform calculations for e.g. the density, which is indispensable for the Kohn-Sham equation. In principle a periodic wave function is transferred by the FFT into a basis with N grid points, squared there (in order to receive in each case the density) and summed up over each i-th band and each wave vector. Finally the inverse FFT takes place, whereby again to the old basis is returned [10]. This is only a very simplified picture, but should illustrate that the plane wave basis introduced above, as well as the FFT have a big role in the calculation.

3.3 k Points

If you want to make calculations with QE, you cannot avoid k points. In the course of the DFT and the numerical calculations the algorithm must evaluate integrals of the following kind:

$$\Xi(\mathbf{k}) = \frac{V_{cell}}{(2\pi)^3} \int_{BZ} \xi(\mathbf{k}) \ d\mathbf{k} \tag{50}$$

There are many numerical methods, which are dedicated to the computation of integrals, as for example the trapezoidal method or the gaussian quadrature, however with these always the question arises, how efficiently they can be implemented numerically [8]. An approach that is widely used today and efficient was developed by Mockhorst and Pack in 1976. In fact QE is based on this method among others. The original paper from the two developers states:

> 'To optimize the calculations it is helpful only to compute these functions at a carefully selected set of points in the BZ'[20].

These points in the BZ, also called k points, are therefore crucial for the evaluation of the integrals mentioned above and thus for the calculation of decisive quantities, such as the total energy of the system. Furthermore, it is possible to increase the efficiency of the integral calculation over the entire BZ by exploiting all existing symmetries. Instead of calculating the integral over the entire BZ, it is also possible to calculate it over the entire Irreducible Brillouin Zone (IBZ) (reduced by all symmetries of the point group of the lattice), which is much faster due to the smaller number of points. The IBZ is then extended in principle to the entire BZ [8].
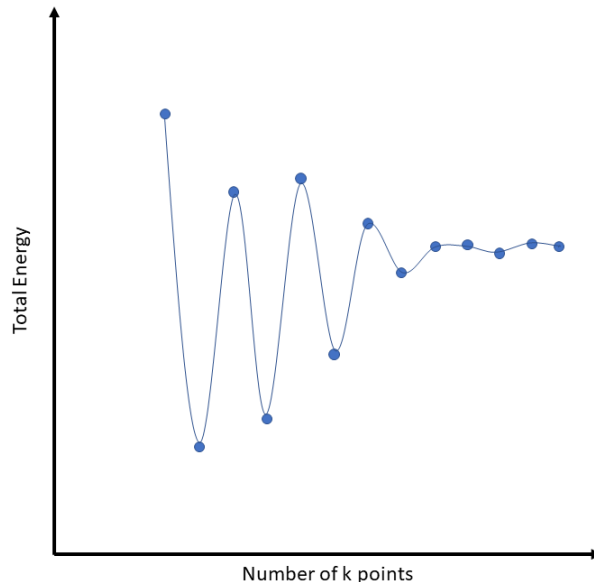

Figure 8: Schematic illustration of the k point convergence test

As you might have guessed, the number of k points has a strong influence on the result. One can assume that with an increased number of k points a more exact

result, but also an increased computational effort and an increased computational time goes along. This is where the term convergence comes into play for the first time. Since one can never know exactly, for which k point set the result is exact enough, but the computation time is lowest, a convergence test must be accomplished before the actual computation. This means that the total energy is plotted as a function of the k-points and then checked for convergence. The convergence is shown by the fact that the total energy settles approximately at one value and deviates only slightly for increasing k-point sets [8]. This situation is illustrated in Fig. 8.

For calculations with hybrid functionals, you must specify a q point set in addition to the k points. This is equivalent to the k point set, but here in relation to the Fock operator. It is important that k+q corresponds to a k point in the k point set [21]. In addition to k point convergence, q point convergence should always be tested. It should be noted, however, that the computation time is also enormously increased here due to a larger q point set.

3.4 Cutoff Energy

Another parameter that influences the result is the plane wave kinetic cut-off energy. The idea is that the Bloch waves are solutions of the Schrödinger equation with the kinetic energy:

$$E = \frac{1}{2}|\mathbf{k} + \mathbf{G}|^2 \tag{51}$$

The solutions with smaller energy must be weighted more heavily because they have a larger physical impact, so solutions with energy greater than $E_{cut} = \frac{1}{2}|\mathbf{G}_{cut}|^2$ are simply truncated. This leads to the fact that the, in principle, infinite plane wave basis is drastically reduced and a faster solution is possible [8].
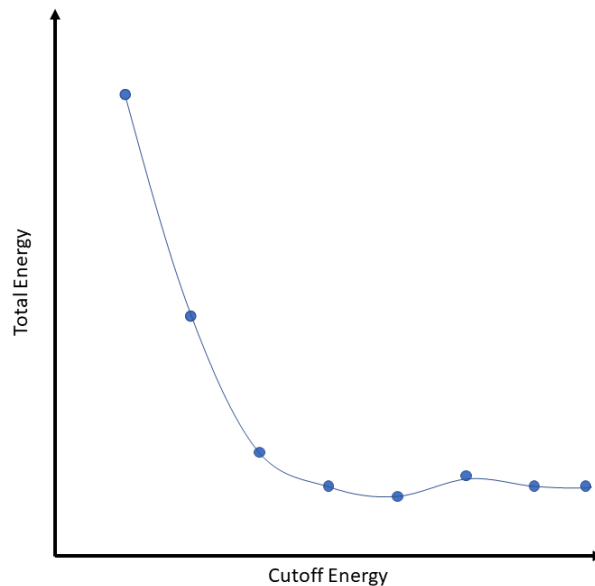

Figure 9: Schematic illustration of the cutoff energy convergence test

As with the k point set, you can never know exactly what the correct cutoff energy is before calculating it. So also here it is necessary to do a convergence test to get solutions which are accurate enough on the one hand, but on the other hand also did not take too much time. This situation is also pictured in Fig. 9.

3.5   Smearing

One more thing that should be addressed is smearing. As already shown in the theory part, metals, semiconductors and insulators have different band structures and different properties. For the latter both, the charge density decreases continuously up to the band gap and the integration over the BZ can be done as described before. Metals, however, exhibit a sharp jump in occupancies at 0K at the Fermi level. In the plane wave representation, it is therefore quite difficult to perform an integration. The idea behind smearing is now to soften this hard edge by a function. This function makes the integrand smoother and thus the integration is easier [15]. There are various functions available, such as Gaussian smearing, Fermi smearing or Methfessel-Paxton smearing.

3.6   Calculation Procedure

3.6.1   Convergence

To test the convergence of the quantities as shown in section 3.3 and section 3.4, several Self-consistent Field (SCF) calculations of the pw.x program from QE have to be performed. To make the work easier, it is useful to know a little about the shell programming language BASH. To avoid having to start each SCF calculation individually and manually, a loop is used in BASH to write the SCF input files for the respective k-points or cut-off energies into a file scf.in and then have QE execute it. Afterwards one can also use a BASH script to write out the total energy from the QE output file scf.out.

3.6.2   Calculation of the band structure with the PBE functional

Once the convergence of the k point and the cutoff energy has been checked, one can continue with the determined values and perform various further calculations. For the calculation of the band structure, a SCF calculation with the converged k point set and the converged cut-off energy is performed. This leads to a more or less correct charge density (compare arguments of convergence). In a further calculation, which is called Non Self-Consistent Field (NSCF), this charge density is then assumed and fixed [22]. In addition, a set of k points is specified, which corresponds to a high symmetry path along which the band structure is to be calculated. The path is based on high symmetry points of the reciprocal cell. In a third calculation, the program bands.x (which is part of the post-processing modul of QE) is used to convert the results of the NSCF calculation into a displayable format. The result is stored in a

.gnu file, which can be displayed by Gnuplot or other programming languages like python.

3.6.3 Calculation of the band structure with Gau-PBE functional

The calculation of the band structure with hybrid functionals is somewhat more difficult, since no NSCF method is implemented. Therefore, maximally localized Wannier functions (MLWFs) are used, which are implemented by the program wannier.x. First, a converged SCF calculation is performed, but for the MLWFs a special k point set is needed (full k point set), which can be generated by the tool kmesh.pl. The k points generated by kmesh.pl are inserted into the scf.in file. After that, the SCF calculation is performed. Next, the Wannier input file is written and executed with the -pp option to generate required files. The pw2wannier90.x is then used for conversion. Finally the actual wannerization is done by executing the Wannier input file without the -pp option. The display can be done again with Gnuplot or another programming language.

4 Results

In this chapter, the band structures for Te are calculated. First, the general structure of Te is dealt with. This is followed by calculations with the PBE functional for comparison purposes. Essentially, it is then about the prediction of the band structure with the Gau-PBE hybrid functional. In both sections, the influence of the SOC is also examined.

4.1 Preliminaries

This section shall contain a brief description of the material to be investigated and the path for the band structure calculation.

4.1.1 Structure

The crystal structure of Te belongs to the space group number $152(P3_121)$. Te can thus be assigned to the trigonal crystal system, with hexagonal Braivais lattice. The unit cell consists of three Te atoms, which are arranged in the cell as follows:
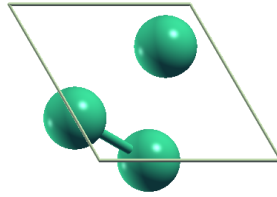
Figure 10: Te in the unit cell

In Fig. 11, Te is shown in a $2 \times 2 \times 7$ supercell. You can see that three atoms, labelled I, II and III, repeat periodically in the material. This type of Te forms helical structures in space by itself. This gives reason to also investigate lower dimensional Te, as Pan et al. have already done [23].
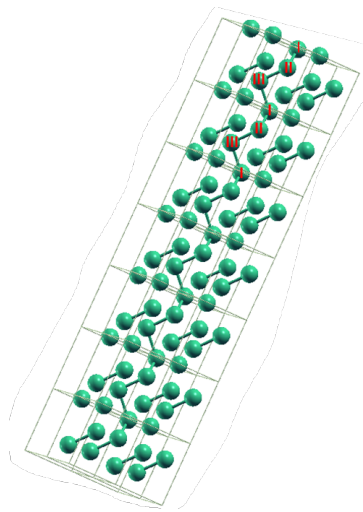

Figure 11: Te in a $2 \times 2 \times 7$ supercell

4.1.2   k Path for band structure Calculations

For the NSCF calculations with the PBE functional, as well as for the Wannierization, it is necessary to specify a path of high symmetry points of the first BZ, along which the band structure is calculated. The points correspond to specific locations of the first BZ and are therefore different for different crystal structures. Fig. 12 shows the hexagonal BZ for the crystal under investigation. The path is marked with green arrows and the labels of the respective points are also noted.
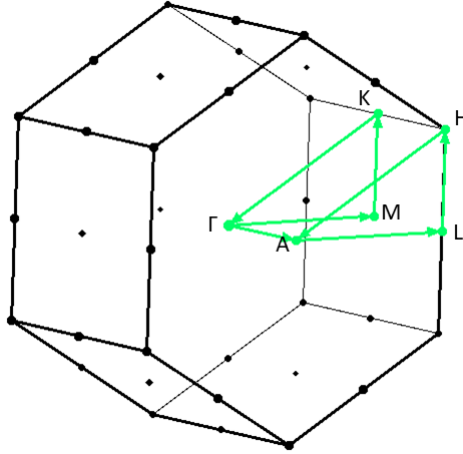
Figure 12: First BZ, as well as the k path for the Te crystal

The path considered is:

$$\Gamma \ \rightarrow \ M \ \rightarrow \ K \ \rightarrow \ \Gamma \ \rightarrow \ A \ \rightarrow \ L \ \rightarrow \ H \ \rightarrow \ A$$

These points will then later also be marked in the band structures on the x-axis.

4.2   Studies with the PBE Functional

4.2.1   Convergence

First, the k point convergence was tested. QE automatically creates a uniform k point set. k point sets were chosen in a range from $6 \times 6 \times 6$ to $30 \times 30 \times 30$, where the step size is two. In addition, an initial estimated cut-off energy of $50 Ry$ was chosen. Since one of the two convergence tests must be started with, one of the two quantities must always be estimated beforehand, since it is not possible to know it beforehand.

The energy for different k point meshes is illustrated in Fig. 13. From a k point set of $14 \times 14 \times 14$ the total energy begins to converge approximately. The fluctuations here are of the order of 10^{-5} Ry or below.

The next step is to examine the total energy as a function of the cut-off energy for convergence. For this purpose, the k point set was fixed at $20 \times 20 \times 20$ and the cut-off energy was varied. This is based on the same scheme as for the k points.
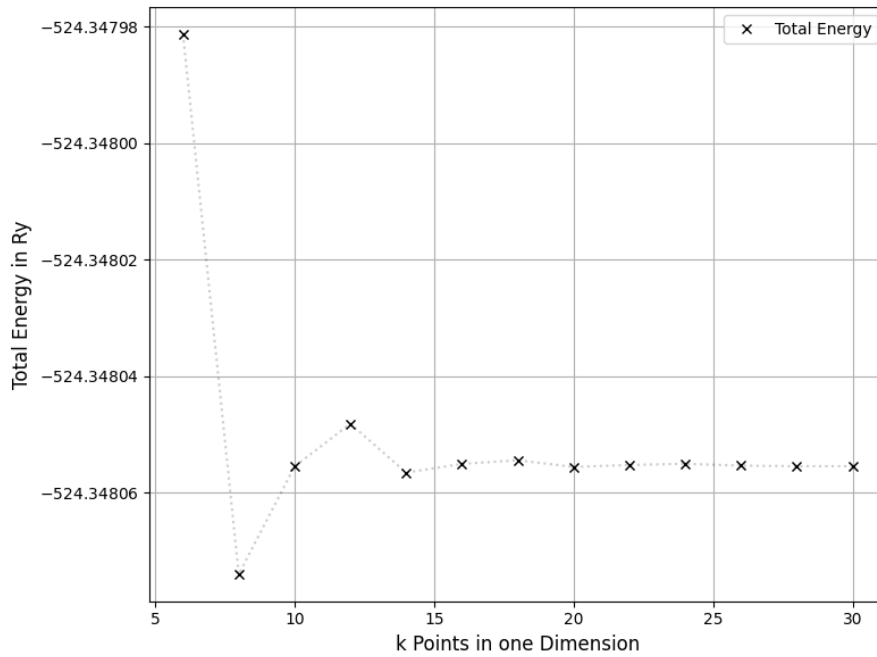
Figure 13: Total energy as a function of the k points as evaluated from DFT (PBE)

Here, a range of $20Ry$ to $140Ry$ was chosen for the cut-off energy. The convergence in Fig. 14 can be clearly seen here. From a value of $40Ry$, the total energy is apparently at the same value.

A cut-off energy of 80Ry was chosen here, which is probably a good middle ground between computational costs and accuracy.
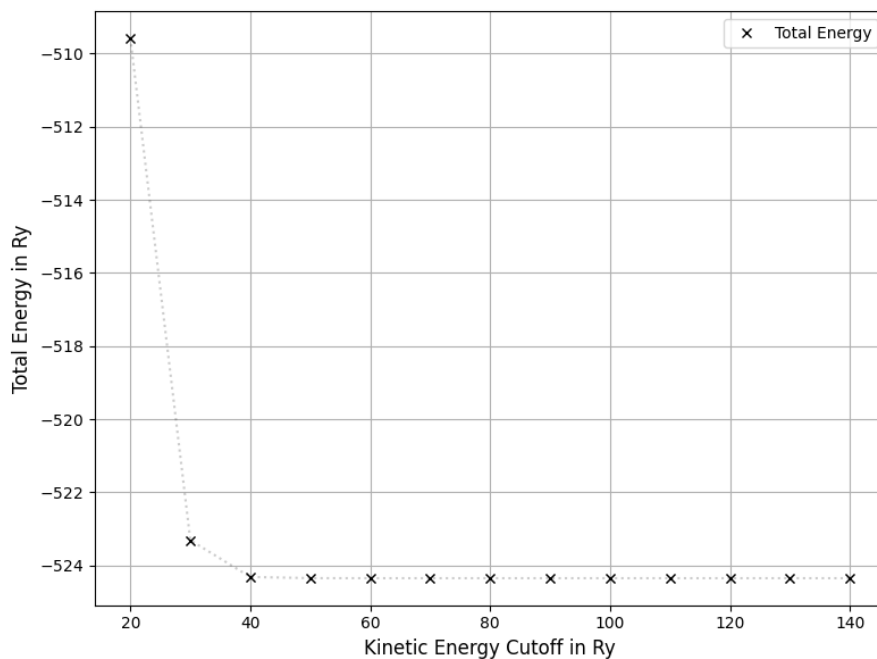

Figure 14: Total energy as a function of the kinetic energy cutoff as evaluated from DFT (PBE)

4.2.2 Band structure without SOC

First, the band structure was calculated without SOC. For this purpose, a fully self-consistent calculation was carried out with the convergence parameters listed here.

The band structure is illustrated in Fig. 15a. The band gap that occurs here is determined by the distance between the valence band maximum and the conduction band minimum at the H point. Fig. 15b shows this area in a magnified image. The maximum of the valence bands slightly differs from the H point. The value of the fundamental gap is 0.1667 eV. The Fermi energy lies between the valence band maximum and the conduction band minimum. Therefore, the calculations at this time and without SOC show that Te is a small gap semiconductor. The result of the band structure is in good agreement with Nakayama et al.[24]. In the calculations of Nakayama et al. a slight offset of the maximum of the valence band can also be recognised.

Furthermore, Pan et al.[23] also performed calculations on bulk Te with the PBE functional and came to the conclusion that without SOC there is an band gap of $0.17eV$. The band gap calculated here is therefore also in good agreement with this reference.

Notwithstanding the good agreement with the references, the band gap is underestimated compared to the experimental value. In 1977, Anzin et al.[25] used the method of photoconductivity spectra to show that Te at a temperature of 1.5 K to 4.2 K has a band gap of (0.3296 ± 0.0009) eV. This means that compared to the band gap of $0.1667eV$, the deviation is approximately $49,4$ %, which is a considerable difference.
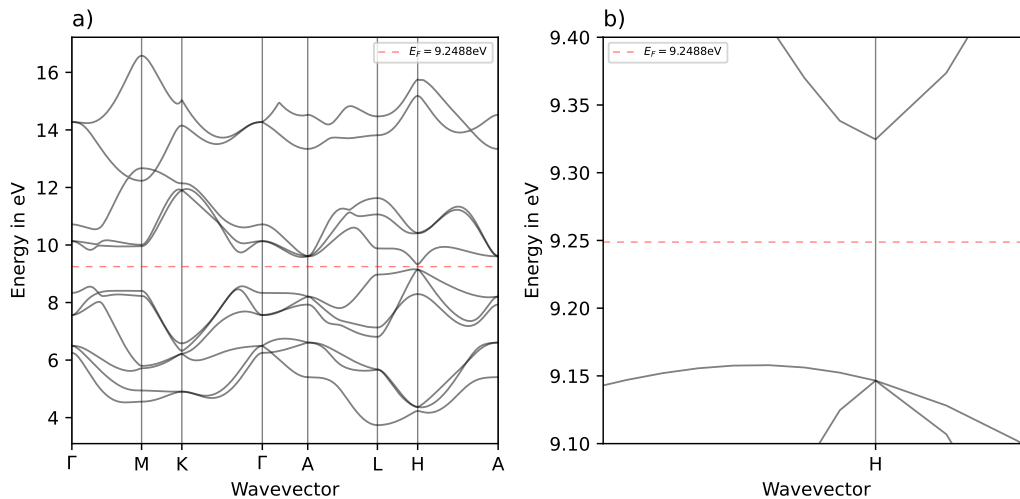

Figure 15: Band structure of Te as obtained from DFT with the PBE functional in presence of SOC

4.2.3 Band Structure with SOC

As a next step we include SOC in the simulations, while leaving other parameters unchanged. The band structure is shown in Fig. 16a.

The larger number of bands, compared to Fig. 15a, results from the lifting of spin degeneracy due to SOC. A zoom is illustrated in Fig. 16b, where is shown that the valence band maximum and the conduction band minimum do not cross or touch each other.
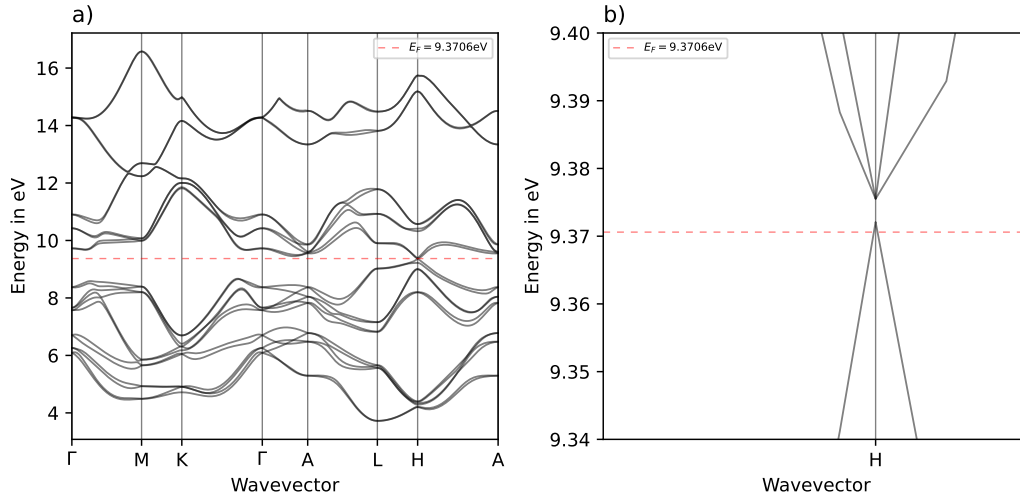

Figure 16: Band structure of Te as obtained from DFT with the PBE functional in absence of SOC

Nevertheless, a small part of the valence band maximum at the H point lies above the Fermi level. This means that the valence band is not completely occupied. Here Te exhibits a metallic character.

The calculated band structure is comparable to the structure worked out by Nakayama et al. [24]. Furthermore, the valence bands around the H point agree with the experimental band structure (compare Fig. 17). Here, ARPES was used to gain insight into the band structure of Te.
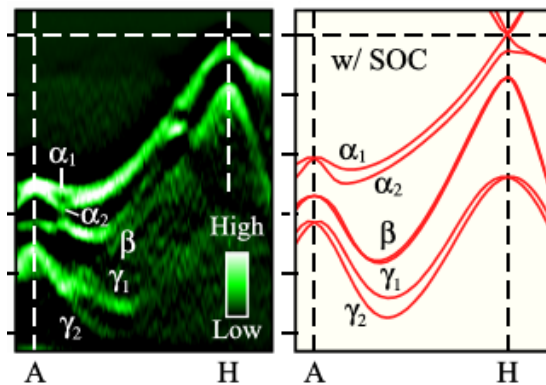

Figure 17: Band structure calculated and measured by Nakayama et al.[24] in presence of SOC

Besides, Pan et al. also carried out a PBE calculation with allowed SOC and arrived at a similar result [23]. They calculated a gap of 0.03 eV at the H point but the fermi energy also lies over the conduction band which indicate a metallic character. The band structures compare well with both references.

4.3   Studies with the Gau-PBE Functional

As shown in the last section, the conventional DFT, i.e. the calculation with GGA xc functionals, fails to predict the band gap at the H point. As was shown in the experiments mentioned earlier, Te has a finite band gap. This could be confirmed in calculations with the GW approximation ([4],[23]). In order to obtain similarly good results, the calculations are carried out in the following with the Gau-PBE hybrid functional, which should lead to a better prediction of the band structure.

4.3.1   Convergence

In this section, it is again first necessary to check for convergence. Since the hybrid functional Gau-PBE is to be used the input files have to be edited. It is now particularly important that convergence is also tested for the q point set (compare section 3.3).
The dependence of the total energy on the k points and the q points is shown in Fig. 18. I consider a much lower number of k points as compared to PBE calculations, since a too fine set of k points in combination with a too fine set of q points would have led to excessive calculation time.
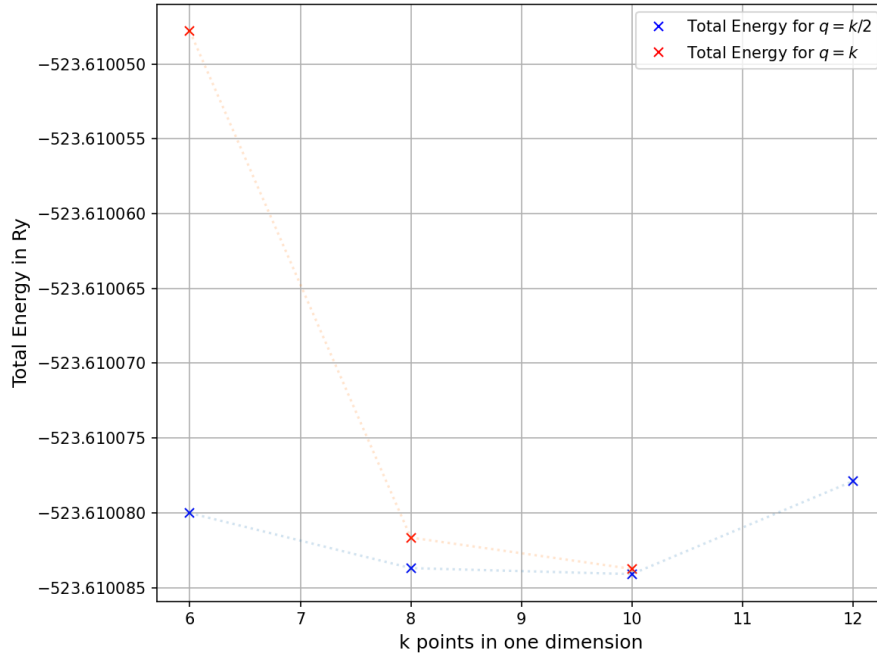

Figure 18: Total energy as a function of the k points, respectively of the q points, as evaluated from hybrid DFT (Gau-PBE)

Furthermore, no total energy could be determined for a k point set of $12 \times 12 \times 12$ and a q point set of $12 \times 12 \times 12$, as the calculation was aborted due to the time limit. The changes of the total energy in Fig. 18 are in the order of 10^{-6} Ry, which is why a k point set of $8 \times 8 \times 8$ and a q point set of $4 \times 4 \times 4$ is considered convergent enough, especially with regard to the computing time.

The convergence of the total energy with respect to the cut-off energy was then tested using the convergent k point set. This was done as already shown in section 4.2.1.
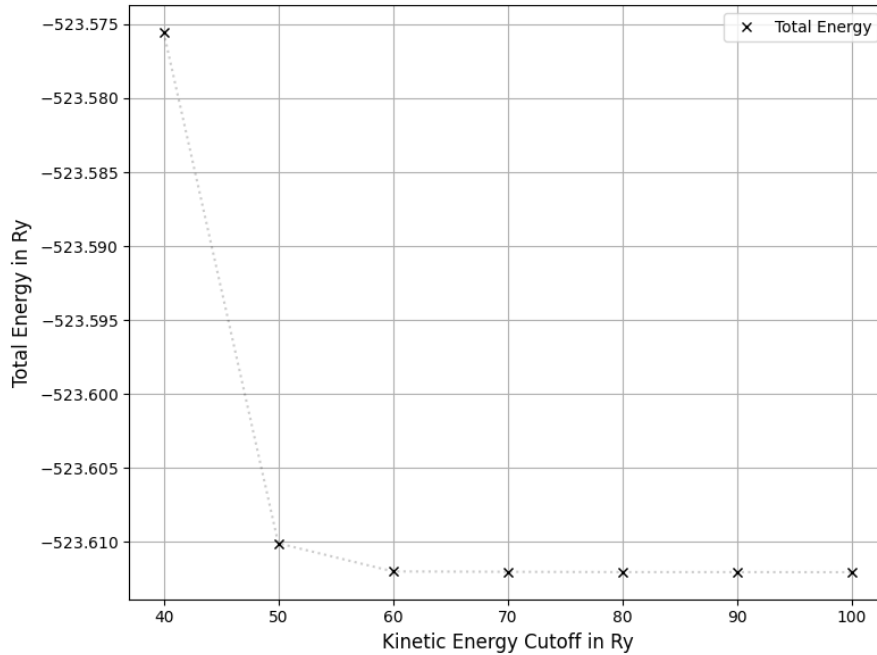

Figure 19: Total energy as a function of the kinetic energy cutoff, as evaluated from hybrid DFT (Gau-PBE)

Here the convergence is again more visible. It starts to converge at a cut-off energy of 60Ry. After that, the fluctuations in the total energy are only marginal. Here, too, there is only a fluctuation in the sixth decimal place. The parameters for the following calculations are therefore a k point set of $8 \times 8 \times 8$, a q point set of $4 \times 4 \times 4$ and a kinetic energy cut-off of $80Ry$

4.3.2 Band Structure without SOC

Also using the Gau-PBE functional, the band structure is first considered without the use of SOC. The band structure is calculated as described in section 3.6.3. As already stated in section 2.2.6, the fraction of HF exchange energy can be changed. In the first step, it is left at the default value of 0.24 for the Gau-PBE functional. After the Wannierization one gets a band structure which is quiet good comparable with the PBE case. The main difference is that the band gap is larger, one can see in comparison to Fig. 15, that the individual bands are somewhat smoother.
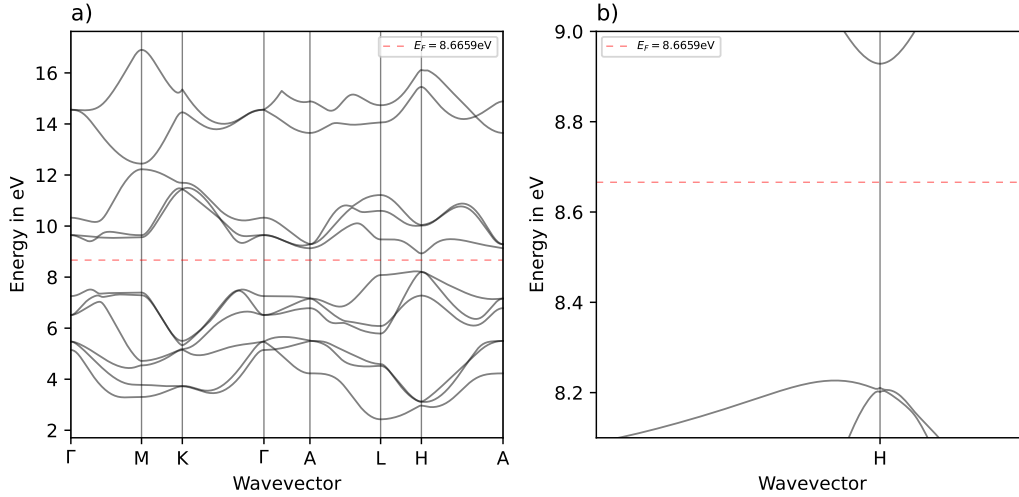
Figure 20: Band structure of Te as obtained from hybrid DFT with the Gau-PBE functional (HF fraction of 0.24) in absence of SOC

A problem that presumably arises from the use of a relative coarse k- and q-point grid and the Wannierization becomes apparent when the band structure is magnified. Fig. 20b shows this issue. Around the H point, the valence band has an unexpected jump, as does the underlying band. The maximum of the valence band is again shifted a minimal distance to the left. This results in a band gap of 0.7016 eV. A comparison with the experimentally measured band gap of 0.3296 eV shows, an overestimation by 0.3720 eV. This suggests that the fraction of the HF exchange energy is too large and a smaller fraction must be chosen to improve agreemure. Accordingly, the influence of the fraction of the HF exchange energy on the band gap is investigated in the following. To do this, the HF exchange energy is varied in small steps and plotted against the bandgap (compare Fig. 21).

As can be seen, the size of the band gap increases with increasing HF fraction. The size of the band gap at a proportion of zero is almost identical to the band gap calculated by the PBE functional (without SOC). This is not surprising since, as described in section 2.2.6, the pure PBE functional is present at an HF fraction of zero. In all calculations, the Fermi level lies between the valence band and the conduction band. Accordingly, Te shows semiconducting properties in all calculations, as in the PBE analysis.

In this case of calculation, according to Fig. 21, one would assume that the band gap at an HF fraction of about 0.09 corresponds to the experimentally calculated band gap. Even though this is a small value, it significantly affects the results of the conventional DFT calculation. With this value of the HF fraction, the band gap of tellurium can be reproduced, however, the calculation was carried out without SOC until now. However, since this has a decisive influence on the band structure, it must be included. Hence, this is done in the same way as in the calculations with the PBE functional in the following section.
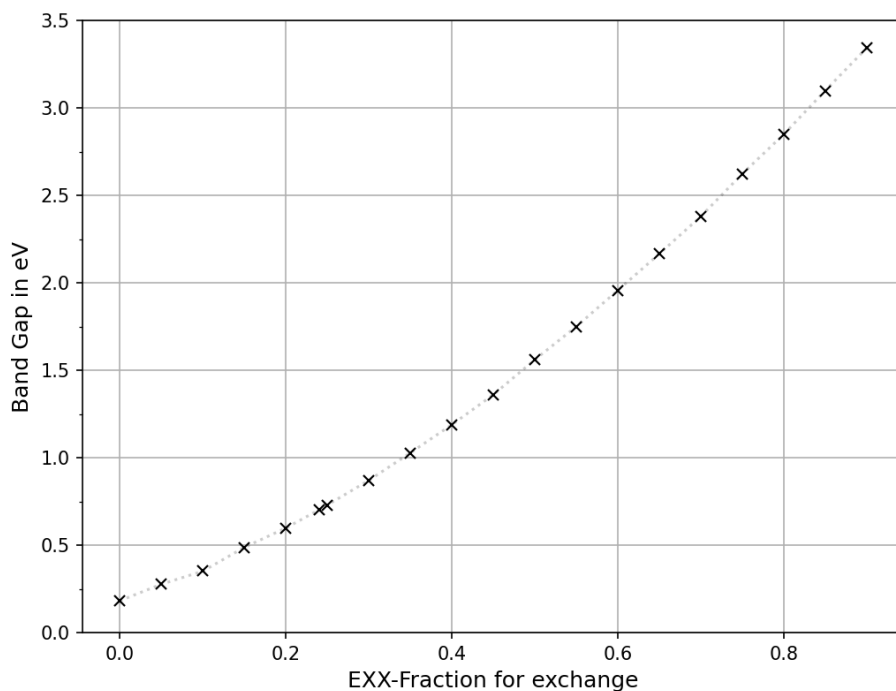
Figure 21: Dependence of the Band Gap on the Exx-Fraction in absence of SOC

4.3.3 Band Structure with SOC

The band structure with the default value for the HF exchange energy was used again to get an overview of the band structure with allowed SOC. This is illustrated in Fig. 22a.
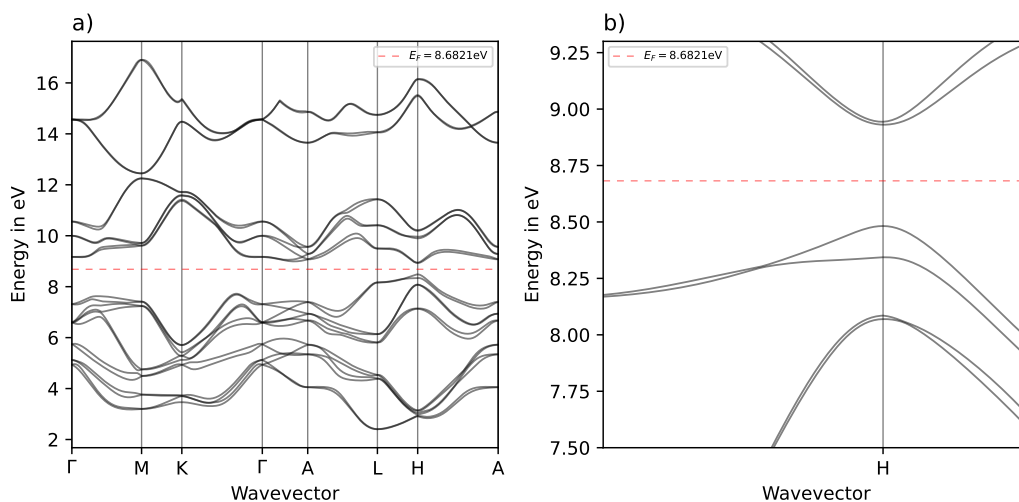

Figure 22: Band structure of Te as obtained from hybrid DFT with the Gau-PBE functional (HF fraction of 0.24) in presence of SOC

The Fermi level also lies between the valence band and the conduction band. With a

band gap of 0.4488 eV, this calculation appears to be closer to the experimental value than the previous hyrid analysis without SOC. The overestimation is only 0.1192 eV. It is also noticeable in the enlargement 22b that the same problems do not occur as in the hybrid calculation without SOC. There are no unexpected jumps around the H point with an HF fraction of 0.24.

The influence of the HF component on the band gap is investigated below. As shown in Fig. 23, the appearance is the same as in the calculation without SOC, reported in Fig. 21. The band gaps are generally smaller than in the calculation without SOC, as expected in analogy to the PBE analysis.

With a fraction of HF exchange energy of almost zero, the material also shows metallic characteristics, since the valence band lies over the fermi energy. This also means that for a low HF fraction, the same band structure can be observed as for pure PBE calculations. It can also be seen that the conduction band minimum is shifted slightly to the right.
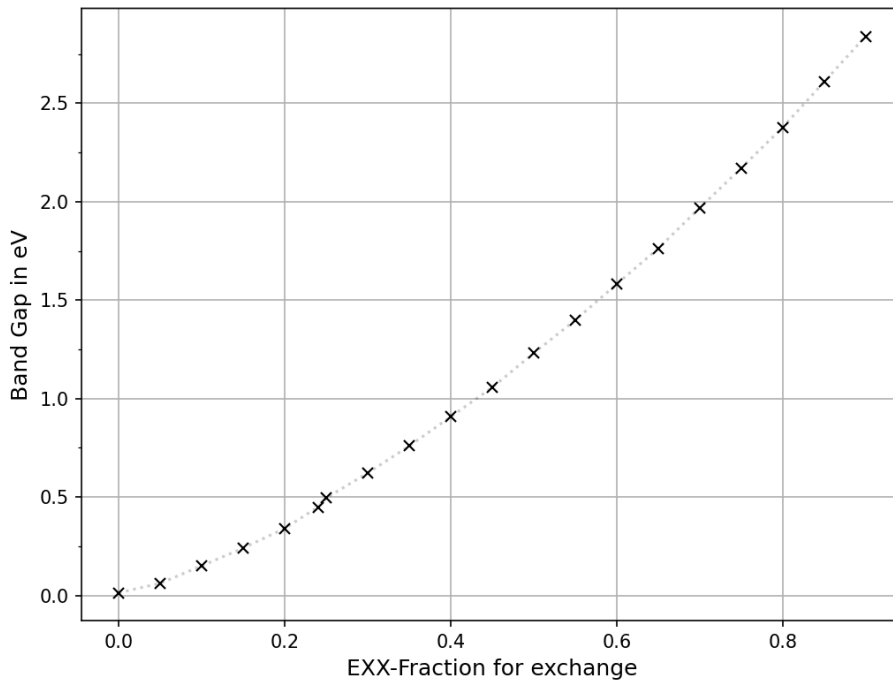

Figure 23: Dependence of the Band Gap on the HF fraction in presence of SOC

If we look at Fig. 23, the question now arises on the one hand as to the fraction of the HF exchange energy at which there is no metallic character but the experimentally confirmed semiconducting character, and at which fraction the value of the experimental band gap is reached.

Regarding the second point it turns out that a HF fraction of 0.194 reproduces the experimentally measured value. The calculated Gap is 0.3296 eV. The band structure is illustrated in Fig. 24. Apart from a slightly different k path, the band structure

calculated here is in good agreement with the band structure calculated by Hirayama et al. especially at the crucial H point (compare Fig. 25), calculated with many-body pertubation theory (GW Approximation).
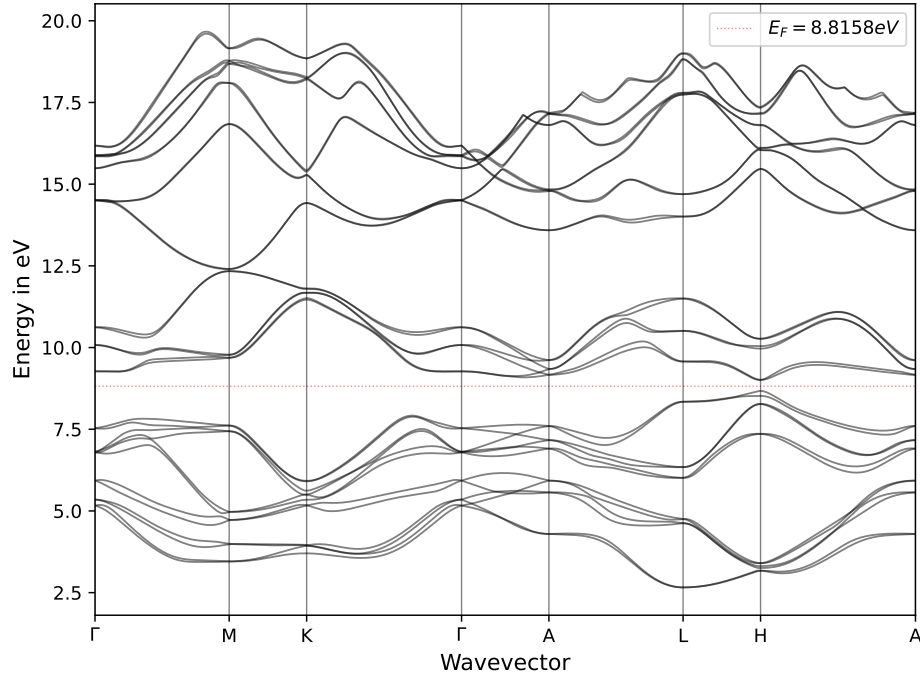

Figure 24: Band structure of Te as obtained from hybrid DFT with the Gau-PBE functional (HF fraction of 0.194) in presence of SOC
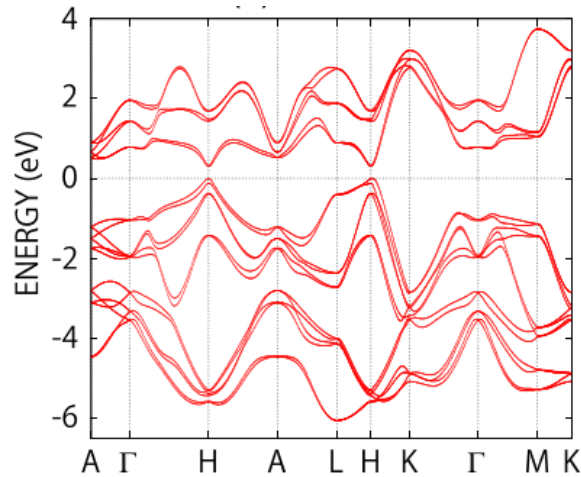

Figure 25: Band structure calculated by Hirayama et al. using many-body pertubation theory (GW approximation) [4]

It remains to be verified at what fraction of the HF exchange energy a transition from the calculated metallic phase to the semiconducting phase takes place. For this

purpose, calculations are carried out again for the values 0.02, 0.03 and 0.04. In all these calculations, the valence band lies over the fermi energy at the H point. Due to insufficient time for the calculations, a more accurate calculation around the value of 0.40 was not performed. It is estimated that the semiconducting phase should begin around a value of 0.42.

A summary can be seen in Fig. 26 respectively. The grey area represents the area where Te shows metallic properties. The area with a green background represents the area where Te behaves like a semiconductor. The experimental value, or the value calculated with an HF fraction of 0.194, is also marked.

The metallic area, because it is so small, is only clearly visible under magnification. There you can see very well that the transition from metallic to semiconducting is fluid. The estimated critical value of the HF fraction of 0.042 should definitely be taken into account in further calculations with a hybrid functional so that the characteristic properties of Te can be reproduced correctly.
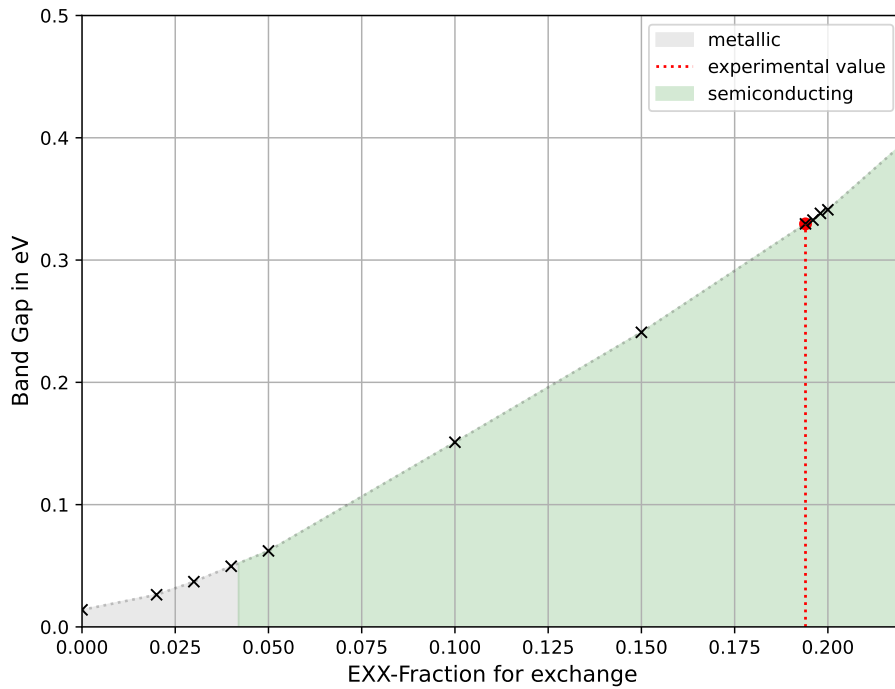

Figure 26: Dependence of the Band Gap on the HF fraction in presence of SOC (magnified)

5 Conclusion/Outlook

In summary, in this thesis the band structure of trigonal Tellurium was investigated. The most important outcome was that the use of the hybrid DFT leads to a band gap which is in accordance to the experimental measured gap. Thus, it could be confirmed that Tellurium is a small gap semiconductor.

The use of DFT as implemented in QE has led to an incorrect prediction of the band gap around the H point. In the absence of SOC the band gap was underestimated, in the presence of SOC trigonal tellurium shows a metallic character, which is due to the fact, that the fermi level cuts through the valence band. This does not correspond to the experimental measurements in either case.

To overcome this problem, the hybrid DFT method was used to obtain a better prediction of the band gap. By changing the HF fraction of the hybrid functional, the band gap around the H point could be determined exactly to the experimental value. It could also be seen here, that at very small values of the HF fraction, Tellurium shows a metallic character.

With regard to the displacive excitation of coherent phonons mentioned in the introduction, the prediction of the band structure is so important because it is precisely the excitation of electrons in excited bands that leads to a decrease in the advantage of the present spiral structure of tellurium, resulting in a new equilibrium position and thus the generation of coherent phonons.

Accordingly, the foundation for further theoretical descriptions of laser-matter interaction, especially with respect to coherent phonons, was laid in this work.

References

[1] E. Eftekhari-Zadeh et al. "Laser energy absorption and x-ray generation in nanowire arrays irradiated by relativistically intense ultra-high contrast femtosecond laser pulses". In: *Physics of Plasmas* 29.1 (Jan. 2022), p. 013301. ISSN: 1070-664X, 1089-7674. DOI: 10.1063/5.0064364. URL: https://aip.scitation.org/doi/10.1063/5.0064364 (visited on 11/22/2022).

[2] P. Tangney and S. Fahy. "Density-functional theory approach to ultrafast laser excitation of semiconductors: Application to the A 1 phonon in tellurium". In: *Physical Review B* 65.5 (Jan. 9, 2002). ISSN: 0163-1829, 1095-3795. DOI: 10.1103/PhysRevB.65.054302. URL: https://link.aps.org/doi/10.1103/PhysRevB.65.054302.

[3] Siqi Lin et al. "Tellurium as a high-performance elemental thermoelectric". In: *Nature Communications* 7.1 (Apr. 2016), p. 10287. ISSN: 2041-1723. DOI: 10.1038/ncomms10287. URL: http://www.nature.com/articles/ncomms10287 (visited on 11/22/2022).

[4] Motoaki Hirayama et al. "Weyl Node and Spin Texture in Trigonal Tellurium and Selenium". In: *Physical Review Letters* 114.20 (May 22, 2015). ISSN: 0031-9007, 1079-7114. DOI: 10.1103/PhysRevLett.114.206401. URL: https://link.aps.org/doi/10.1103/PhysRevLett.114.206401.

[5] F. Giustino. *Materials modelling using density functional theory: prop-erties and predictions*. 1st ed. Oxford: Oxford University Press, 2014. ISBN: 978-0-19-966243-2. DOI: 10.1080/00107514.2015.1100218.

[6] V. Fock. "Näherungsmethode zur Lösung des quantenmechanischen Mehrkörperproblems". In: *Zeitschrift für Physik* 61.1 (Jan. 1, 1930), pp. 126–148. ISSN: 0044-3328. DOI: 10.1007/BF01340294.

[7] C.B. Lang and N. Pucker. *Mathematische Methoden in der Physik*. Berlin, Heidelberg: Springer Berlin Heidelberg, 2016. ISBN: 978-3-662-49312-0. DOI: 10.1007/978-3-662-49313-7. URL: http://link.springer.com/10.1007/978-3-662-49313-7 (visited on 10/26/2022).

[8] D.S. Sholl and J.A. Steckel. *Density Functional Theory: A Practical Introduction*. New Jersey: A John Wiley and Sons, 2009. ISBN: 978-0-470-37317-0.

[9] P. Hohenberg and W. Kohn. "Inhomogeneous Electron Gas". In: *Physical Review* 136.3 (Nov. 9, 1964), B864–B871. ISSN: 0031-899X. DOI: 10.1103/PhysRev.136.B864. URL: https://link.aps.org/doi/10.1103/PhysRev.136.B864 (visited on 10/29/2022).

[10] R. M. Martin. *Electronic Structure: Basic Theory and Practical Methods*. 2nd ed. Cambridge: Cambridge University Press, 2020. ISBN: 978-1-108-42990-0. DOI: 10.1017/CBO9780511805769.

[11] John P. Perdew, Kieron Burke, and Yue Wang. "Generalized gradient approximation for the exchange-correlation hole of a many-electron system". In: *Physical Review B* 54.23 (Dec. 15, 1996), pp. 16533–16539. ISSN: 0163-1829, 1095-3795. DOI: 10.1103/PhysRevB.54.16533. URL: https://link.aps.org/doi/10.1103/PhysRevB.54.16533 (visited on 11/12/2022).

[12] Matthias Ernzerhof and Gustavo E. Scuseria. "Assessment of the Perdew–Burke–Ernzerhof exchange-correlation functional". In: *The Journal of Chemical Physics* 110.11 (Mar. 15, 1999), pp. 5029–5036. ISSN: 0021-9606, 1089-7690. DOI: 10.1063/1.478401. URL: http://aip.scitation.org/doi/10.1063/1.478401 (visited on 11/12/2022).

[13] Jong-Won Song and Kimihiko Hirao. "Efficient method of evaluation for Gaussian Hartree-Fock exchange operator for Gau-PBE functional". In: *The Journal of Chemical Physics* 143.2 (July 14, 2015), p. 024102. ISSN: 0021-9606, 1089-7690. DOI: 10.1063/1.4923264. URL: http://aip.scitation.org/doi/10.1063/1.4923264 (visited on 11/11/2022).

[14] R. Gross and A. Marx. *Festkörperphysik*. 3rd ed. De Gruyter, 2018. ISBN: 978-3-11-055918-7. DOI: 10.1524/9783110358704.

[15] J.G. Lee. *Computational Materials Science: An Introdcution*. 2nd ed. Boca Raton: CRC Press, 2017. ISBN: 978-1-498-74973-2.

[16] D. R. Hamann. "Optimized norm-conserving Vanderbilt pseudopotentials". In: *Physical Review B* 88.8 (Aug. 19, 2013), p. 085117. ISSN: 1098-0121, 1550-235X. DOI: 10.1103/PhysRevB.88.085117. URL: https://link.aps.org/doi/10.1103/PhysRevB.88.085117 (visited on 11/13/2022).

[17] Martin Schlipf and François Gygi. "Optimization algorithm for the generation of ONCV pseudopotentials". In: *Computer Physics Communications* 196 (Nov. 2015), pp. 36–44. ISSN: 00104655. DOI: 10.1016/j.cpc.2015.05.011. URL: https://linkinghub.elsevier.com/retrieve/pii/S0010465515001897 (visited on 11/13/2022).

[18] Peter Scherpelz et al. "Implementation and Validation of Fully Relativistic *GW* Calculations: Spin–Orbit Coupling in Molecules, Nanocrystals, and Solids". In: *Journal of Chemical Theory and Computation* 12.8 (Aug. 9, 2016), pp. 3523–3544. ISSN: 1549-9618, 1549-9626. DOI: 10.1021/acs.jctc.6b00114. URL: https://pubs.acs.org/doi/10.1021/acs.jctc.6b00114 (visited on 11/13/2022).

[19] Quantum Espresso. *FAQ Pseudopotentials*. 2022. URL: https://www.quantum-espresso.org/faq/faq-pseudopotentials/#2.5 (visited on 11/13/2022).

[20] H. J. Monkhorst and J. D. Pack. "Special points for Brillouin-zone integrations". In: *Physical Review B* 13.12 (June 15, 1976), pp. 5188–5192. ISSN: 0556-2805. DOI: 10.1103/PhysRevB.13.5188. URL: https://link.aps.org/doi/10.1103/PhysRevB.13.5188 (visited on 11/13/2022).

[21]   P. Giannozzi. *PW Examples EXX*. 2017. URL: `https://gitlab.com/QEF/q-e/-/tree/develop/PW/examples/EXX_example` (visited on 11/13/2022).

[22]   A. Ferretti and D. Varsano. *Non self-consistent calculations: Band structures and Density Of States*. 2021. URL: `http://wiki.max-centre.eu/index.php/Non_self-consistent_calculations:_Band_structures_and_Density_Of_States` (visited on 11/15/2022).

[23]   Yuanyuan Pan et al. "Dependence of excited-state properties of tellurium on dimensionality: From bulk to two dimensions to one dimensions". In: *Physical Review B* 98.8 (Aug. 22, 2018), p. 085135. ISSN: 2469-9950, 2469-9969. DOI: `10.1103/PhysRevB.98.085135`. URL: `https://link.aps.org/doi/10.1103/PhysRevB.98.085135` (visited on 11/18/2022).

[24]   K. Nakayama et al. "Band splitting and Weyl nodes in trigonal tellurium studied by angle-resolved photoemission spectroscopy and density functional theory". In: *Physical Review B* 95.12 (Mar. 22, 2017). ISSN: 2469-9950, 2469-9969. DOI: `10.1103/PhysRevB.95.125204`.

[25]   V. B. Anzin et al. "Measurement of the energy gap in tellurium under pressure". In: *Physica Status Solidi (a)* 42.1 (July 16, 1977), pp. 385–390. ISSN: 00318965, 1521396X. DOI: `10.1002/pssa.2210420143`. URL: `https://onlinelibrary.wiley.com/doi/10.1002/pssa.2210420143` (visited on 11/18/2022).

Affidavit

I declare that I have prepared my bachelor thesis '*Ab-initio study on the electronic properties of trigonal Tellurium*' independently and without the use of other than the stated aids and that I have marked all passages that I have taken verbatim or in spirit from publications as such. I agree that the work will be checked with the help of plagiarism checking software. The work has not previously been submitted to any examination authority in the same or similar form or in excerpts.

I certify that the written version submitted is the same as the version saved on the enclosed media.

Eidesstattliche Erklärung

Ich erkläre, dass ich meine Bachelorarbeit '*Ab-initio study on the electronic properties of trigonal Tellurium*' selbstständig und ohne Benutzung anderer als der angegebenen Hilfsmittel angefertigt und alle Stellen, die ich wörtlich oder sinngemäß aus Veröffentlichungen übernommen habe, als solche kenntlich gemacht habe. Ich erkläre mich damit einverstanden, dass die Arbeit mit Hilfe einer Plagiatsprüfungssoftware überprüft wird. Die Arbeit wurde in gleicher oder ähnlicher Form oder in Auszügen noch bei keiner Prüfungsbehörde eingereicht.

Ich versichere, dass die eingereichte schriftliche Fassung mit der auf dem beiliegenden Datenträger gespeicherten Fassung übereinstimmt.

_____

(Date, Sign)